



Published in final edited form as:

Nat Chem Biol. 2021 January ; 17(1): 113–121. doi:10.1038/s41589-020-00679-1.

Bi-paratopic and multivalent VH domains block ACE2 binding and neutralize SARS-CoV-2

Colton J. Bracken¹, Shion A. Lim¹, Paige Solomon¹, Nicholas J. Rettko¹, Duy P. Nguyen^{1,6}, Beth Shoshana Zha², Kaitlin Schaefer¹, James R. Byrnes¹, Jie Zhou¹, Irene Lui¹, Jia Liu^{1,7}, Katarina Pance¹, QCRG Structural Biology Consortium

Caleigh M. Azumaya, Christian Billesbølle, Axel F. Brilot, Melody G. Campbell, Amy Diallo, Miles Sasha Dickinson, Devan Diwanji, Meghna Gupta, Nadia Herrera, Nick Hoppe, Huong T. Kratochvil, Yanxin Liu, Gregory E. Merz, Henry C. Nguyen, Carlos Nowotny, Michelle Moritz, Tristan W. Owens, Sergei Pourmal, Cristina Puchades, Alexandra N. Rizo, Ursula Schulze-Gahmen, Amber M. Smith, Ming Sun, Erron W. Titus, Iris D. Young, Jianhua Zhao, Daniel Asarnow, Justin Biel, Alisa Bowen, Julian R. Braxton, David Bulkley, Jen Chen, Cynthia M. Chio, Un Seng Chio, Ishan Deshpande, Loan Doan, Bryan Faust, Sebastian Flores, Mingliang Jin, Kate Kim, Victor L. Lam, Fei Li, Junrui Li, Yen-Li Li, Yang Li, Xi Liu, Megan Lo, Kyle E. Lopez, Liam McKay, Arthur A. Melo, Frank R. Moss III, Phuong Nguyen,

Users may view, print, copy, and download text and data-mine the content in such documents, for the purposes of academic research, subject always to the full Conditions of use: http://www.nature.com/authors/editorial_policies/license.html#terms

*Corresponding Author: jim.wells@ucsf.edu.

QCRG Structural Biology Consortium.

In addition to those listed explicitly in the author contributions, the structural biology portion of this work was performed by the QCRG (Quantitative Biosciences Institute Coronavirus Research Group) Structural Biology Consortium. Listed below are the contributing members of the consortium listed by teams in order of team relevance to the published work. Within each team the team leads are italicized (responsible for organization of each team, and for the experimental design utilized within each team), then the rest of team members are listed alphabetically. **CryoEM grid freezing/collection team:** *Caleigh M. Azumaya, Cristina Puchades, Ming Sun*, Julian R. Braxton, Axel F. Brilot, Meghna Gupta, Fei Li, Kyle E. Lopez, Arthur Melo, Gregory E. Merz, Frank Moss, Joana Paulino, Thomas H. Pospiech, Jr., Sergei Pourmal, Alexandra N. Rizo, Amber M. Smith, Paul V. Thomas, Feng Wang, Zanolin Yu. **CryoEM data processing team:** *Miles Sasha Dickinson, Henry C. Nguyen*, Daniel Asarnow, Julian R. Braxton, Melody G. Campbell, Cynthia M. Chio, Un Seng Chio, Devan Diwanji, Bryan Faust, Meghna Gupta, Nick Hoppe, Mingliang Jin, Fei Li, Junrui Li, Yanxin Liu, Gregory E. Merz, Joana Paulino, Thomas H. Pospiech, Jr., Sergei Pourmal, Smriti Sangwan, Raphael Trenker, Donovan Trinidad, Eric Tse, Kaihua Zhang, Fengbo Zhou. **Mammalian cell expression team:** *Christian Billesbølle, Melody G. Campbell, Devan Diwanji, Carlos Nowotny, Amber M. Smith, Jianhua Zhao*, Caleigh M. Azumaya, Alisa Bowen, Nick Hoppe, Yen-Li Li, Phuong Nguyen, Cristina Puchades, Mali Safari, Smriti Sangwan, Kaitlin Schaefer, Raphael Trenker, Tsz Kin Martin Tsui, Natalie Whitis. **Protein purification team:** *Daniel Asarnow, Michelle Moritz, Tristan W. Owens, Sergei Pourmal*, Caleigh M. Azumaya, Cynthia M. Chio, Bryan Faust, Meghna Gupta, Kate Kim, Joana Paulino, Jessica K. Peters, Kaitlin Schaefer, Tsz Kin Martin Tsui. **Crystallography team:** *Nadia Herrera, Huong T. Kratochvil, Ursula Schulze-Gahmen, Iris D. Young*, Justin Biel, Ishan Deshpande, Xi Liu. **Bacterial expression team:** *Amy Diallo, Meghna Gupta, Erron W. Titus*, Jen Chen, Loan Doan, Sebastian Flores, Mingliang Jin, Huong T. Kratochvil, Victor L. Lam, Yang Li, Megan Lo, Gregory E. Merz, Joana Paulino, Aye C. Thwin, Zanolin Yu, Fengbo Zhou, Yang Zhang. **Infrastructure team:** David Bulkley, Arceli Joves, Almarie Joves, Liam McKay, Mariano Tabios, Eric Tse. **Leadership team:** *Oren S. Rosenberg, Kliment A. Verba*, David A. Agard, Yifan Cheng, James S. Fraser, Adam Frost, Natalia Jura, Tanja Kortemme, Nevan J. Krogan, Aashish Manglik, Daniel R. Southworth, Robert M. Stroud. The QCRG Structural Biology Consortium has received support from: Quantitative Biosciences Institute, Defense Advanced Research Projects Agency HR0011-19-2-0020 (to D.A.A. and K.A.V.; B. Shoichet PI), FastGrants COVID19 grant (K.A. Verba PI), Laboratory For Genomics Research (O.S. Rosenberg PI) and Laboratory For Genomics Research (R.M. Stroud PI)

Author Contributions:

C.J.B. and D.P.N. designed and constructed the VH-phage library. C.J.B., S.A.L., N.J.R., J.Z., I.L., J.L., K.P. cloned, expressed, and purified the VH binders and/or antigens. C.J.B., S.A.L., J.L. designed and/or conducted the in vitro characterization of the VH binders. J.R.B. designed and conducted the competition ELISA assay with convalescent patient sera. P.S., N.J.R., S.A.L. designed and conducted the pseudovirus neutralization assays. P.S., N.J.R., B.S.Z., S.A.L. designed and conducted the live virus neutralization assays. K.S. prepared samples for cryo-EM and the QCRG SBC performed cryo-EM data collection and analyses. S.A.L., X.X.Z., K.K.L., J.A.W. led the coordination of external collaborations and supervised the project. C.J.B., S.A.L., J.A.W. co-wrote the manuscript with input from all the authors.

Competing Interests:

The authors declare no competing interests.

Joana Paulino, Komal Ishwar Pawar, Jessica K. Peters, Thomas H. Pospiech Jr., Maliheh Safari, Smriti Sangwan, Kaitlin Schaefer, Mariano Tabios, Paul V. Thomas, Aye C. Thwin, Raphael Trenker, Donovan Trinidad, Eric Tse, Tsz Kin Martin Tsui, Feng Wang, Natalie Whitis, Zanlin Yu, Kaihua Zhang, Yang Zhang, Fengbo Zhou, Oren S Rosenberg, Kliment A Verba, David A Agard, Yifan Cheng, James S Fraser, Adam Frost, Natalia Jura, Tanja Kortemme, Nevan J Krogan, Aashish Manglik, Daniel R. Southworth, Robert M Stroud³, Xin X. Zhou¹, Kevin K. Leung¹, James A. Wells^{1,4,5,*}

¹Department of Pharmaceutical Chemistry, University of California San Francisco, San Francisco, California, 94158, USA.

²Department of Pulmonary, Critical Care, Allergy and Sleep Medicine, University of California San Francisco, San Francisco, CA 94158, USA.

³Quantitative Biosciences Institute (QBI) Coronavirus Research Group Structural Biology Consortium, University of California San Francisco, San Francisco, CA 94158, USA.

⁴Department of Cellular & Molecular Pharmacology, University of California San Francisco, San Francisco, California, 94158, USA.

⁵Chan Zuckerberg Biohub, San Francisco, CA 94158, USA

⁶Present address: Lyell Immunopharma Inc., Seattle, WA 98109, USA

⁷Present address: Merck & Co., South San Francisco, CA 94080, USA

Abstract

Neutralizing agents against SARS-CoV-2 are urgently needed for the treatment and prophylaxis of COVID-19. Here, we present a strategy to rapidly identify and assemble synthetic human variable heavy (VH) domains toward neutralizing epitopes. We constructed a VH-phage library and targeted the angiotensin-converting enzyme 2 (ACE2) binding interface of the SARS-CoV-2 Spike receptor-binding domain (Spike-RBD). Using a masked selection approach, we identified VH binders to two non-overlapping epitopes and further assembled these into multivalent and bi-paratopic formats. These VH constructs showed increased affinity to Spike (up to 600-fold) and neutralization potency (up to 1400-fold) on pseudotyped SARS-CoV-2 virus when compared to standalone VH domains. The most potent binder, a trivalent VH, neutralized authentic SARS-CoV-2 with half-maximal inhibitory concentration (IC₅₀) of 4.0 nM (180 ng/mL). A cryo-EM structure of the trivalent VH bound to Spike shows each VH domain engaging an RBD at the ACE2 binding site, confirming our original design strategy.

Introduction:

The emergence of SARS-CoV-2 and the associated COVID-19 disease has emphasized the need to rapidly generate therapeutics against novel pathogens. SARS-CoV-2 enters cells through the interaction of the viral Spike receptor-binding domain (Spike-RBD) and host angiotensin-converting enzyme-2 (ACE2) on the surface of lung epithelial cells.¹ Antibody and antibody-like biologics that can block this interaction are promising therapeutic candidates because of their high specificity and neutralization potency.² The majority of antibodies isolated so far against SARS-CoV-2, SARS-CoV-1, and MERS are derived

from screening B-cells of infected patients or repurposed from animal immunizations.^{3–7} These approaches, though effective, can be time-consuming and may not necessarily yield neutralizing antibodies. Given the pressing nature of this pandemic, there is a need for multiple parallel strategies to rapidly produce potent, recombinant, and neutralizing biologics.

In vitro display technologies using yeast or phage are well-established approaches for generating high-affinity binders from large naïve libraries.⁸ *In vitro* selection can be done without infected individuals and only requires the recombinant protein target. One of the recently developed modalities are small single domain antibodies derived from variable heavy homodimer (VHH) domains of antibodies from camels or llamas, often referred to as nanobodies, and are usually obtained by camelid immunization and B-cell cloning.^{9–12} Nanobodies have some advantages. Their single-chain and small size (11 to 15 kDa) allow them to bind epitopes or penetrate tissues that may not be accessible to monoclonal antibodies (mAbs) (150 kDa), and nanobodies can be rapidly produced in *E. coli*.^{13,14} However, nanobodies derived from animal immunization can also suffer from long-turnaround times. Although this can be overcome with synthetic nanobody libraries,^{15,16} nanobody scaffolds that are animal-derived raise significant concerns regarding immunogenicity. More recently, variable heavy (VH) domains derived from human scaffolds have been produced and tested against a number of targets.^{17–19}

Thus, we and others have been interested in developing VH binders to SARS-CoV-2 for the present pandemic, and as a test case for future ones.^{20–23} However, one limitation of synthetic single domain binders is that as monomers, they often lack the strong binding affinity necessary for therapeutic application. Affinity maturation can improve this, although this extends the development timeline. Instead, generating linked multivalent or multi-paratopic VH binders could be a more rapid approach to utilize avidity to boost affinity and efficacy.²⁴ Linking VH domains into such homo- and hetero-bifunctional formats is more straightforward than preparing similar multifunctional antibodies because the latter requires correct heavy and light chain pairing to maintain binding affinity, whereas multifunctional VH domains have no such requirements.¹¹

Here, we constructed a human VH-phage library derived from the clinically approved trastuzumab scaffold and validated its use on multiple antigens. By utilizing a masked phage selection strategy, we rapidly identified VH domains at two non-overlapping epitopes within the ACE2 binding site of the SARS-CoV-2 Spike-RBD. By linking these VH domains with a strategic linker into bi-paratopic and multivalent binders, we improved affinity from mid-nM to ~100 pM without any additional high-resolution structural information. These high-affinity binders are capable of potently neutralizing pseudotyped and live SARS-CoV-2. A cryo-electron microscopy (cryo-EM) structure of the most potent trivalent VH bound to Spike shows that each VH domain precisely targets the ACE2 binding interface on all three RBDs of Spike. We believe our VH-phage library and this multivalent and multi-paratopic approach is highly advantageous to target distinct epitopes within an antigen and can be broadly applied to other viral and non-viral targets to leverage avidity for increased potency.

Results:

Construction of a synthetic human VH-phage library

To enable the generation of single-domain antibodies against targets such as SARS-CoV-2 Spike, we designed a synthetic VH-phage library using the VH domain (4D5) from the highly stable and clinically successful trastuzumab antibody (Fig. 1a).^{25,26} The VH scaffold was modified to include five amino acid changes predicted to reduce aggregation (Supplementary Table 1).²⁷ To bias toward colloidal stability, aspartate and arginine or glutamate residues were inserted at the beginning and at two or three terminal positions of CDR H1, as these have been previously used to improve aggregation resistance of VH and scFv fragments from the VH3 germline.^{19,28} Diversity was introduced into CDR H1 and CDR H2 using a minimalistic approach where variability was largely restricted to tyrosine and serine residues (Extended Data Fig. 1).²⁹ We introduced high-diversity mixtures of amino acids into CDR H3 because it is usually critical to antigen recognition (Extended Data Fig. 1), and Fab-phage libraries with highly diverse CDR H3 sequences have successfully yielded high-affinity antibodies to a variety of target antigens.^{30,31} Furthermore, charged polar residues such as aspartate were introduced at 10% frequency to decrease net surface hydrophobicity to mitigate aggregation and decrease the propensity for non-specific binders in the library.

Based on previous designs, we chose loop length variations of 5 to 7 residues in CDR H1 and 6 to 20 residues in CDR H3 while CDR H2 was kept constant at 17 residues (Kabat definitions) (Extended Data Fig. 1, Supplementary Table 2).^{30,32} To cover this large sequence space with a minimal bias towards different length variants, five separate sub-libraries were constructed by binning CDR H3 loop length insertions (X₂₋₁₆) in incremental sets of three and combined to yield a final library of $\sim 5 \times 10^{10}$ transformants (Supplementary Figure 1). Analysis of the unique CDR H3 sequences by next-generation sequencing (NGS) showed that observed amino acid frequencies closely matched our designs and all CDR H3 length variants were represented in the final library (Fig. 1b–d, Supplementary Figure 2). Finally, to test the performance of the library, several rounds of panning were performed on representative antigens including both cytosolic and membrane proteins. These panning experiments were done in parallel with an in-house Fab-phage library. For all target antigens, high levels of enrichment were observed (Supplementary Figure 3). For the majority of antigens, enrichment levels were comparable or substantially higher for the VH-phage library compared to the Fab-phage library.

Identification of VHs that target multiple epitopes

To date, most neutralizing mAbs against SARS-CoV-2 target Spike, and not surprisingly many of the most potent target the ACE2 binding interface.^{3,7} While cryo-EM structures show that the ACE2 binding interface remains largely solvent-accessible in both the RBD “up” and “down” conformations,³³ simultaneous intra-molecular engagement by both binding arms of mAbs may be challenging as they are not geometrically arranged to engage multiple RBDs on a single Spike trimer. Thus, our goal was to target this highly neutralizing epitope with VHs and subsequently link them together to utilize avidity beyond that of a homo-bivalent mAb.

We first expressed the Spike-RBD (residues 328–533) and the ACE2 peptidase domain (residues 1–640) as biotinylated Fc-fusions for VH-phage selections.³⁴ To specifically enrich for VH-phage that bind the ACE2 binding site on Spike-RBD, the library was first cleared with the Spike-RBD-Fc/ACE2-Fc complex to remove phage that bound outside the ACE2 binding interface. This was followed by selection on Spike-RBD-Fc alone to enrich for phage that bound the unmasked ACE2 binding site (Fig. 2a). By rounds 3 and 4, significant enrichments for phage that bound Spike-RBD-Fc but not to Spike-RBD-Fc/ACE2-Fc complex were observed (Supplementary Figure 4a). Single clones were isolated and characterized for their ability to bind Spike-RBD-Fc by phage enzyme-linked immunosorbent assays (ELISA) (Supplementary Figure 4b). Nearly all VH-phage showed enhanced binding to Spike-RBD-Fc over the Spike-RBD-Fc/ACE2-Fc complex, suggesting they bound the same epitope as ACE2 and could potentially block this interaction (Supplementary Figure 4c). In total, 85 unique VH-phage sequences were identified, and a subset was characterized as recombinant VH domains. We identified three lead VH candidates that bound Spike-RBD with K_D values ranging from 23–113 nM (Fig. 2b–d). These VH were specific to Spike-RBD and did not recognize other in-house antigens (Extended Data Fig. 2). Epitope binning demonstrated that the three VH domains mapped to two non-overlapping epitopes we call Site A and Site B within the larger ACE2 binding site (Supplementary Figure 5). The VH domain that recognizes Site A (A01) binds independently from the VHs that recognize Site B (B01 and B02) (Fig. 2e–2h).

Bi-paratopic and multivalent linkage increases affinity

We chose two parallel approaches to increase the affinity of the VH binders to Spike through avidity. First, we reasoned that VHs targeting Site A or Site B are in close proximity because they are non-overlapping but compete for the larger ACE2 binding site. Therefore, these VHs could be linked together to engage the same RBD simultaneously and improve affinity through intra-RBD avidity. Using the three VH monomers (A01, B01, B02) as modular units, we generated two bi-paratopic linked dimers (VH₂) by fusing A01 with B01 or B02 (Fig. 3a). In a parallel approach, we aimed to leverage the trimeric nature of Spike and engage multiple RBDs on the same Spike simultaneously to improve affinity through inter-RBD avidity. To that end, we generated mono-paratopic Fc fusions (VH-Fc), linked dimers (VH₂), and linked trimers (VH₃) (Fig. 3a). The VH₂ and VH₃ consisted of a C-to-N terminal fusion of two or three VH monomers via a 20-amino acid Gly-Ser linker (~70 Å) while the VH-Fc consisted of a fusion of VH to the human IgG1 Fc domain via a flexible Fc hinge (~100 Å). The structure of the SARS-CoV-2 Spike trimer suggests the linked VH domains could bridge the distance between RBDs on an individual Spike (<55 Å), but are unlikely to span RBDs between discrete Spike proteins based on the inter-Spike distance on the viral envelope (150–180 Å) (Extended Data Fig. 3).^{33,35}

ELISA and BLI binding assays to Spike-RBD show that the VH-Fc, VH₂, and VH₃ have 2.7 to 600-fold higher affinity to Spike-RBD (K_D = 0.1–8.4 nM) compared to the standalone VH monomers (Fig. 3b–d, Extended Data Fig. 4, Supplementary Table 3 and 4, Supplementary Figure 6). Interestingly, fold-increases in affinity were greater for binders that target Site B or both Site A and Site B combined. The most potent constructs bound trimeric Spike ectodomain (S_{ecto}) with K_D s in the hundreds of picomolar range and all

utilized VH B01 (Fig. 3b–d). Next, we examined whether these multivalent VH can block ACE2 binding to Spike by testing several high-affinity constructs (VH-Fcs; VH₂ A01-B01, VH₂ A01, and VH₂ B02) in a sequential BLI binding assay. S_{ecto} was immobilized on the biosensor, pre-blocked with each VH binder, and then assayed for binding to ACE2-Fc (Fig. 3e). We found that all binders tested substantially blocked binding of ACE2-Fc to S_{ecto}. Similarly, we examined whether these engineered VH-Fcs can compete with SARS-CoV-2 Spike-reactive antibodies in convalescent patient serum. Using a competition ELISA format previously developed by our group,³⁶ we found that VH-Fcs reduced the binding of patient antibodies to SARS-CoV-2 Spike-RBD (Fig. 3f). Taken together these data show that modular reformatting of these VH domains can significantly increase the affinity to Spike and block the same immunogenic epitopes as patient-derived Abs.

Lastly, we characterized the biophysical properties of these engineered VH by differential scanning fluorimetry (DSF), size exclusion chromatography (SEC), and reconstitution after lyophilization. The VH binders can be expressed in *E. coli* at high yields (i.e. VH₂ A01-B01 and VH₃ B01 express at ~1 g/L in shake flask culture) and have good stabilities (T_m = 56–65 °C) (Supplementary Figure 7). The most potent binders elute as a single monodisperse peak via SEC (Supplementary Figure 8), and VH₃ B01 retains binding to Spike-RBD and a monodisperse SEC profile after lyophilization and reconstitution suggesting it could be suitable for lyophilized formulation (Supplementary Figure 9).

Bi-paratopic and multivalent VH neutralize virus

SARS-CoV2 is a biosafety level 3 (BSL3) pathogen. To facilitate studies under routine laboratory conditions, we utilized a pseudotyped lentiviral (HIV) particle that has been previously reported.³⁷ These pseudotyped particles are generated from a three-plasmid system containing non-Env proteins from HIV, a luciferase reporter, and the SARS-CoV-2 spike protein. Entry of this viral particle into ACE2-expressing target cells and neutralization by anti-Spike antibodies have previously been shown to faithfully recapitulate features of the authentic pathogen without the need for working under BSL3 conditions. This pseudotyped virus was used to determine the half-maximal inhibitory concentration (IC₅₀) of neutralization for each construct.

The VH monomers neutralized pseudotyped virus weakly (IC₅₀ > 50 nM), and cocktails of unlinked monomers did not improve potency. In contrast, the multivalent binders (VH₂, VH₃, and VH-Fc) neutralized ~10–1000 fold more potently compared to their respective monomeric units (Fig. 4a, Supplementary Table 5, Extended Data Fig. 5). There was a linear correlation between the in vitro binding affinity (K_D) to Spike-RBD and the pseudotyped neutralization potency (IC₅₀) across the different binders (R^2 = 0.72) (Fig. 4b).

In particular, we observed that bi-paratopic VH₂ A01-B01 and VH₂ A01-B02 were stronger neutralizers than unlinked monomer cocktails. Additionally, the neutralization curves of the bi-paratopic (multi-site) VH₂ differed from the homodimeric (single-site) VH₂ binding to either Site A or B. That is, the bi-paratopic VH₂ exhibited a more cooperative transition and fully neutralized virus, while the homodimeric VH₂ showed a more linear transition and did not fully block viral entry even at high concentrations (Fig. 4c). This may reflect mechanistic differences; the bi-paratopic VH₂ can theoretically engage a single RBD using

both VH domains simultaneously (intra-RBD avidity) and more fully occlude the ACE2 binding site, while the homodimeric VH₂ must bridge separate RBDs within the trimer (inter-RBD avidity).

Furthermore, the increase in neutralization potency as we increase the number of tandem VH units is exemplified by the VH B01-derived binders, as the IC₅₀s of VH₂ B01 and VH₃ B01 are two to three orders of magnitude lower than the IC₅₀ of the VH B01 monomer (Fig. 4d). This is also observed for VH-Fc B01, which also neutralizes two orders of magnitude more potently than the monomer. Interestingly, although the neutralization potency of VH₂ A01 is better than VH A01, the potency does not improve further when a third domain is added (VH₃ A01), indicating that epitope-specific geometries can affect the extent to which increasing valency improves potency. The pseudotyped virus neutralization assays demonstrate that the top predicted binders from *in vitro* affinity data, VH₂ A01-B01, VH₂ A01-B02, VH₃ B01, and VH-Fc B01 are indeed the most potent with IC₅₀s of 0.74 nM, 1.08 nM, 0.156 nM, and 1.86 nM, respectively.

Lastly, we tested the ability of the most potent VH binders to neutralize authentic SARS-CoV-2 virus. As predicted, VH₃-B01 neutralized most potently. The VH-Fc B01, VH₂ A01-B01, and VH₂ A01-B02 followed trends consistent with both the *in vitro* binding K_D and pseudotyped virus IC₅₀. VH₃ B01, VH-Fc B01, VH₂ A01-B01, and VH₂ A01-B02 blocked authentic SARS-CoV-2 viral entry with IC₅₀s of 3.98 nM, 33.5 nM, 12.0 nM, and 26.2 nM, respectively (Fig. 4e, Supplementary Table 6).

Cryo-EM confirms multivalent binding of VH₃ B01 to Spike

To confirm whether our linking strategy could successfully engage multiple RBDs on Spike, we obtained a 3.2 Å global resolution cryo-EM 3D reconstruction of SARS-CoV-2 S_{ecto} in complex with VH₃ B01, the most potent neutralizer (Fig. 5a, Extended Data Fig. 6, Supplementary Figure 10, Supplementary Table 7). Although the S2 region of S_{ecto} was resolved at the reported resolution, the RBDs with the bound VH domains were resolved at about 6 Å resolution. However, even at this resolution the structure unambiguously revealed the three RBDs on Spike are in a two “up” and one “down” conformation. Densities corresponding to each VH domain are present on all three RBDs, indicating that VH B01 can bind both “up” and “down” conformations of RBD. SARS-CoV-2 Spike is rarely observed in this conformation with most structures being in all RBD “down” state or one RBD “up” state.^{4,6,33,38} The binding epitope of VH B01 overlaps with the known ACE2 binding site (Fig. 5b), confirming the intended mechanism of neutralization and validating the ability of the masked selection strategy to precisely direct a binder toward the intended surface on a target protein. To further investigate the dependence of binding on Spike conformation, we performed BLI experiments with S_{ecto} at pH 4.5, which has been recently reported to lock Spike in an “all-down” RBD conformation.³⁹ Binding of both VH₃ B01 and VH₂ A01-B01 to S_{ecto} were greatly diminished (Extended Data Fig. 7). This observation suggests that one or more RBDs in the “up” conformation may be required for VH B01 to access multiple RBDs on Spike.

Discussion:

Here we describe a straightforward strategy to rapidly generate linked single-domain binders that potentially neutralize SARS-CoV-2. We began by creating and validating a diverse human VH-phage library and generating VH binders to the ACE2 binding interface of Spike-RBD by a masked selection approach. From a panel of 85 unique VH binders, three were identified that recognized two separate epitopes within the ACE2 binding interface with nM affinity. In order to engage multiple epitopes simultaneously within an RBD or across RBDs on Spike, these VH monomers were linked into multivalent and bi-paratopic formats by Gly-Ser linkers or Fc domains without any further high-resolution structural information. This linkage approach not only significantly enhanced affinity, but also substantially improved the viral neutralization potency. We confirmed the basis of this increase by obtaining a cryo-EM structure of the most potent trivalent VH bound to Spike. Consistent with our original design, the trivalent VH simultaneously blocked the ACE2 binding site on all three RBDs of Spike.

We show that *in vitro* binding affinities and neutralization potencies against this oligomeric target can be dramatically increased with valency. This is exemplified by VH B01, which shows a 460-fold increase in binding affinity and 1400-fold increase in pseudotyped virus neutralization from VH B01 to VH₂ B01 to VH₃ B01. The cryo-EM structure of VH₃ B01 shows this binder neutralizes SARS-CoV-2 by blocking the ACE2 binding site on all three RBDs on Spike. Although there could be other contributing neutralization mechanisms such as viral aggregation induced by inter-Spike or inter-virion binding by the multivalent VH, the relatively short linker length (20 amino acids) between the VH domains would make these long-distance interactions significantly less likely. Additionally, no aggregates or S_{ecto} multimers induced by VH₃ B01 were observed during cryo-EM sample preparation and data collection, which further suggests that inter-Spike or inter-virion binding effects, if present, are minimal.

A similar relationship between valency and potency is observed for VH B02, which also targets the same epitope (Site B). However, VH A01, which targets Site A, is mechanistically distinct as there is no change in potency between a bivalent (VH₂) and a trivalent (VH₃) format. This suggests that unlike Site B binders, the trivalent Site A binder may not be able to fully engage all 3 RBDs. This could be due to the specific binding mechanism and epitope of VH A01, conformational differences of the RBDs within the Spike trimer, or spatial constraints of the linker. Structure determination of Site A binders in complex with Spike can elucidate the mechanistic and geometric difference between Site A and Site B epitopes. Additionally, structure-guided approaches to optimize linker lengths and orientations, coupled with an affinity maturation campaign may enable further increases in potency beyond what is demonstrated in this study.

Interestingly, we observed a difference in the cooperativity of the pseudotyped virus neutralization curves between bivalent VH₂ that target both Site A and Site B (bi-paratopic) versus VH₂ that target only Site A or Site B (mono-paratopic). Despite similar IC₅₀s, the IC₉₅s for bi-paratopic VH₂ (VH₂ A01-B01, VH₂ A01-B02) were much lower than mono-paratopic VH₂ binders. This could indicate a mechanistic difference between these

two types of bi-valent binders. Bi-valent VH₂ can engage multiple RBD, but only 2 of the 3 RBDs can be efficiently occluded, leaving one RBD accessible to ACE2. This could underlie why the neutralization of mono-paratopic VH₂ does not reach 100% compared to say, a trivalent VH₃. Curiously, however, the bi-paratopic VH₂ can fully neutralize virus, despite also having only two VH domains. We reason that intra-RBD avidity may play an important and unique role in the neutralization mechanism of bi-paratopic VH₂. Mono-paratopic binders are limited to inter-RBD avidity and regardless of valency are limited to up to 3 binding sites on Spike. In contrast, bi-paratopic VH₂ can utilize up to 6 binding epitopes on Spike and utilize both inter-RBD and intra-RBD avidity. Additionally, a more complete occlusion of the ACE2 binding interface (~864 Å²)⁴⁰ on RBD by the bi-paratopic VH₂ could also underlie this difference in neutralization profiles. Although we do not have a structure of VH₂ A01-B01, we know both A01 and B01 can bind simultaneously within the ACE2 binding site. The cryo-EM structure for B01 shows good coverage of the ACE2 binding site (Fig. 5B) while leaving open adjacent space for VH A01 to occupy a non-overlapping epitope. A better understanding of the binding and neutralization mechanisms of bi-paratopic binders remain a current area of investigation and could lead to the engineering of more potent, multi-specific binders.

Previous studies that utilized designed ankyrin repeat proteins (DARPin)s, llama derived nanobodies, computationally designed proteins, and bivalent Fabs inspired our engineering strategy.^{41–47} We believe our human-derived VH domains offer distinct advantages. Foremost, they would not require the time-consuming structure-guided humanization process that would be necessary for therapeutic nanobody development. Additionally, the VH domains derived from our library have favorable biophysical properties derived from a shared well-behaved scaffold. Our most potent construct, VH₃ B01, retains high-affinity binding after lyophilization cycles. This factor coupled with scalable production in bacterial systems may enable lung delivery via inhalation and could facilitate rapid deployment in response to a pandemic. Despite these advantages, single-domain binders have comparatively lower stability and *in vivo* half-life than mAbs, and due to their novelty, pharmacodynamic properties, such as the prevalence of anti-drug antibodies, have not been as extensively tested in the clinic. Despite these challenges, the engineering potential of these single-domain binders is immense and provides an exciting avenue for the next generation of therapeutic antibody engineering and development. Our results illustrate this potential through a straightforward and rapid strategy to improve the efficacy of single-domain binders and could be applied to other protein interfaces of interest, including future viral proteins and other antigens associated with human disease.

Methods:

VH Library Construction and Validation by NGS

The VH-phage library was created through bivalent display of VH on the surface of M13 bacteriophage as has been previously described.^{30,48,49} In brief, the DNA phagemid library was created through oligonucleotide mutagenesis. First, the human VH-4D5 sequence was modified with five mutations (35G/39R/45E/47L/50R) in the framework and with restriction sites in each of the CDRs: AgeI in CDR H1, NcoI in CDR H2, and XhoI in

CDR H3 (Supplementary Table 1). Oligonucleotides were synthesized by a custom Trimer Phosphoramidite mix for CDR H1 and CDR H2 (Twist Bioscience) and CDR H3 (Trilink Biotechnologies, Inc.) (Supplementary Table 2). After mutagenesis DNA sublibrary pools were digested with appropriate restriction enzymes to remove the phagemid template before transformation into SS320 electrocompetent cell (Lucigen) for phage production. NGS of the CDR H3 was performed on the pooled library by amplifying the phagemid from boiled phage with in-house primers. Samples were submitted for analysis on a HiSeq4000 (Illumina) with a custom primer: TGAGGACACTGCCGTCTATTATTGTGCTCGC ($T_m = 67^\circ\text{C}$, GC% = 52). NGS analysis of output was performed using an in-house informatics pipeline written in R. In brief, the raw NGS data sequencing file (*.fastq.gz) was converted into a table comprised of the DNA sequences, the amino acid sequences (CDR H3), and the counts/frequency as columns and then saved as a *.csv file for further analysis (e.g., calculation of: amino acid abundance, sequence logo, H3 length distribution, etc.). Several filters were applied: i) low-quality sequences containing “N” were removed, ii) sequences with any stop codon were removed; iii) only the sequences that were in-frame were kept. Scripts are available for download at: https://github.com/crystaljie/VH_library_CDR_H3_NGS_analysis_Cole.Bracken.git.

Cloning, Protein Expression, and Purification

Spike-RBD-monomer, Spike-RBD-Fc, Spike ectodomain (S_{ecto}), and ACE2-Fc were produced as biotinylated proteins as previously described.³⁴ VH were subcloned from the VH-phagemid into an *E. coli* expression vector pBL347. VH₂ and VH₃ were cloned into pBL347 with a 20-amino acid Gly-Ser linker. VH-Fc were cloned into a pFUSE (InvivoGen) vector with a human IgG1 Fc domain. All constructs were sequence verified by Sanger sequencing. VH, VH₂, and VH₃ constructs were expressed in *E. coli* C43(DE3) Pro + using an optimized autoinduction media and purified by protein A affinity chromatography similarly to Fabs (Supplementary Figure 11).³⁰ VH-Fc were expressed in Expi293 BirA cells using transient transfection (Expifectamine, Thermo Fisher Scientific). Four days after transfection, the media was harvested, and VH-Fc were purified using protein A affinity chromatography. All proteins were buffer exchanged into PBS by spin concentration and stored in aliquots at -80°C . The purity and integrity of proteins were assessed by SDS-PAGE. All proteins were endotoxin removed using an endotoxin removal kit (Thermo Fischer) prior to use in neutralization assays.

Phage selection with VH-phage library

Phage selections were done according to previously established protocols.³⁰ Selections were performed using biotinylated antigens captured with streptavidin-coated magnetic beads (Promega). In each round, the phage pool was first cleared by incubation with beads loaded with 500 nM ACE2-Fc/Spike-RBD-Fc complex. The unbound phage were then incubated with beads loaded with Spike-RBD-Fc. After washing, the bound phage was eluted by the addition of 2 $\mu\text{g}/\text{mL}$ of TEV protease. In total, four rounds of selection were performed with decreasing amounts of Spike-RBD-Fc as indicated in Figure 2A. All steps were done in PBS buffer + 0.02% Tween-20 + 0.2% BSA (PBSTB). Individual phage clones from the third and fourth round of selections were analyzed by phage ELISA.

Phage ELISA

For each phage clone, 4 different conditions were tested—Direct: Spike-RBD-Fc, Competition: Spike-RBD-Fc with an equal concentration of Spike-RBD-Fc in solution, Negative selection: ACE2-Fc/Spike-RBD-Fc complex, and Control: Fc. 384-well Nunc Maxisorp flat-bottom clear plates (Thermo Fisher Scientific) were coated with 0.5 µg/mL of NeutrAvidin in PBS overnight at 4°C and subsequently blocked with PBS + 0.02% Tween-20 + 2% BSA for 1 hr at room temperature. Plates were washed 3X with PBS containing 0.05% Tween-20 (PBST) and were washed similarly between each of the steps. 20 nM of biotinylated Spike-RBD-Fc, ACE2-Fc/Spike-RBD-Fc complex, or Fc diluted in PBSTB was captured on the NeutrAvidin-coated wells for 30 min, then blocked with PBSTB + 10 µM biotin for 30 min. Phage supernatant diluted 1:5 in PBSTB were added for 20 min. For the competition samples, the phage supernatant was diluted into PBSTB with 20 nM Spike-RBD-Fc. Bound phage were detected by incubation with anti-M13-HRP conjugate (Sino Biological)(1:5000) for 30 min, followed by the addition of TMB substrate (VWR International). The reaction was quenched with the addition of 1 M phosphoric acid and the absorbance at 450 nm was measured using a Tecan M200 Pro spectrophotometer.

ELISA EC50 with Spike-RBD-monomer

384-well Nunc Maxisorp flat-bottom clear plates were prepared similarly to the phage ELISA protocol (above) by coating with neutravidin, followed by blocking with PBST + 2% BSA, incubation with 20 nM Spike-RBD-monomer, and blocking by PBSTB + 10 µM biotin. VH binders in 4-fold dilutions ranging from 500 nM to 2.8 pM were added for 1 hour. Bound VH was detected by incubation with Protein A HRP conjugate (Thermo Fischer Scientific) (1:10,000) for 30 min, followed by the addition of TMB substrate for 5 min, quenching by 1 M phosphoric acid, and detection of absorbance at 450 nm. Each concentration was tested in duplicate, and the assay was repeated three times.

Bio-layer interferometry (BLI) Experiments

Bio-layer interferometry data (BLI) were measured using an Octet RED384 (ForteBio) instrument. Spike-RBD or S_{ecto} were immobilized on a streptavidin or Ni-NTA biosensor and loaded until a 0.4 nm signal was achieved. After blocking with 10 µM biotin, purified binders in solution was used as the analyte. PBSTB was used for all buffers for BLI at pH 7.4. For BLI at pH 4.5, 10 mM sodium acetate pH 4.5, 150 mM NaCl, 0.2 mg/mL BSA and 0.01% (w/v) Tween-20 was used. Data were analyzed using the ForteBio Octet analysis software and kinetic parameters were determined using a 1:1 monovalent binding model.

Competition ELISA with COVID-19 convalescent patient sera

Competition ELISA with convalescent patient sera was conducted with the same patient sera as previously reported.³⁶ Samples were collected in accordance with the Declaration of Helsinki using protocols approved by the UCSF Institutional Review Board (Protocol 20–30338). Patients were voluntarily recruited based on their history of prior SARS-CoV-2 infection. All patients provided written consent. Patient sera were de-identified prior to delivery to the Wells Lab, where all experiments presented here were performed. Briefly, sera were obtained as described from patients with a history of positive nasopharyngeal

SARS-CoV-2 RT-PCR test and at least 14 days after the resolution of their COVID-19 symptoms. Healthy control serum was obtained prior to the emergence of SARS-CoV-2. Sera were heat-inactivated (56°C for 60 min) prior to use. Competitive serology using biotinylated SARS-CoV-2 Spike-RBD as the capture antigen was performed as previously reported with slight modifications.³⁶ Instead of supplementing sera diluted 1:50 in 1% nonfat milk with 100 nM ACE2-Fc, 100 nM of each of the indicated VH-Fc fusions was used. Bound patient antibodies were then detected using Protein L-HRP (Thermo Fisher Scientific 32420, [1:5000]). Background from the raw ELISA signal in serum-treated wells was removed by first subtracting the signal measured in NeutrAvidin-alone coated wells then subtracting the signal detected in antigen-coated wells incubated with 1% nonfat milk + 100 nM competitor.

Differential Scanning Fluorimetry (DSF)

DSF was conducted as previously described.³⁰ Briefly, purified protein was diluted to 0.5 μ M or 0.25 μ M in buffer containing Sypro Orange 4x (Invitrogen) and PBS and assayed in a 384-well white PCR plate. All samples were tested in duplicate. In a Roche LC480 LightCycler, the sample was heated from 30°C to 95°C with a ramp rate of 0.3°C per 30 sec and fluorescence signal at 490 nm and 575 nm were continuously collected. T_m was calculated using the Roche LC480 LightCycler software.

Size Exclusion Chromatography (SEC)

SEC analysis was performed using an Äkta Pure system (GE Healthcare) using a Superdex 200 Increase 10/300 GL column. 100 μ L of 2–3 mg/mL of each analyte was injected and run with a constant mobile phase of degassed 10 mM Tris pH 8.0 200 mM NaCl. Absorbance at 280 nm was measured. The post-lyophilization and reconstitution SEC was performed using an Agilent HPLC 1260 Infinity II LC System using an AdvanceBio SEC column (300 Å, 2.7 μ m, Agilent). Fluorescence (excitation 285 nm, emission 340 nm) was measured.

Preparation of SARS-CoV-2 pseudotyped virus and HEK-ACE2 overexpression cell line

HEK293T-ACE2 cells were a gift from Arun Wiita's laboratory at the University of California, San Francisco. Cells are cultured in D10 media (DMEM + 1% Pen/Strep + 10% heat-inactivated FBS). Plasmids to generate pseudotyped virus were a gift from Peter Kim's lab at Stanford University and SARS-Cov-2 pseudotyped virus was prepared as previously described.³⁷ Briefly, plasmids at the designated concentrations were added to OptiMEM media with FuGENE HD Transfection Reagent (Promega) at a 3:1 FuGENE:DNA ratio, incubated for 30 min, and subsequently transfected into HEK-293T cells. After 24 hrs, the supernatant was removed and replaced with D10 culture media. Virus was propagated for an additional 48 hrs, and the supernatant was harvested and filtered. Virus was stored at 4°C for up to 10 days.

HEK-ACE2 were seeded at 10,000 cells/well on 96-well white plates (Corning, cat. 354620). After 24 hrs, pseudotyped virus stocks were titrated via a two-fold dilution series in D10 media, and 40 μ L were added to cells. After 60 hrs, infection and intracellular luciferase signal was determined using Bright-Glo™ Luciferase Assay (Promega), and the dilution achieving maximal luminescent signal within the linear range, $\sim 3\text{--}5 \times 10^5$

luminescence units, was chosen as the working concentration for neutralization assays. Pseudovirus stocks were flash-frozen in aliquots and stored at -80°C and thawed on ice just prior to use in a neutralization assay.

Pseudotyped viral neutralization assays

HEK-ACE2 were seeded at 10,000 cells/well in 40 μL of D10 on 96-well white plates (Corning, cat. 354620) 24 hours prior to infection. To determine IC_{50} for pseudotyped virus, dose series of each VH binder were prepared at 3x concentration in D10 media and 50 μL were aliquoted into each well in 96-well plate format. Next, 50 μL of virus diluted in D10 media were added to each well and the virus and blocker solution was allowed to incubate for 1 hr at 37°C . Subsequently, 80 μL of the virus and blocker solution were transferred to wells seeded with HEK-ACE2. After 60 hrs of infection at 37°C , intracellular luciferase signal was measured using the Bright-Glo™ Luciferase Assay. 80 μL of reconstituted Bright-Glo™ luciferase reagent was added to each well, incubated at room temperature with gentle shaking for 5 min, before the luminescence was measured on a Tecan M200 pro spectrophotometer. The half-maximal inhibitory concentration (IC_{50}) was determined using a 4-parameter nonlinear regression (GraphPad Prism).

Authentic Viral Neutralization Assays

Authentic virus neutralization assays were done as previously described.³⁴ All handling and experiments using live SARS-CoV-2 virus clinical isolate 2019-nCoV/USA-WA1/2020 (BEI Resources) was conducted under Biosafety Level 3 containment with approved BUA and protocols. VeroE6 cells were cultured in Minimal Essential Media (MEM), 10% FBS, 1% Pen-Strep. For neutralization assays, VeroE6 cells were seeded on 6-well culture plates at $3.8\text{E}5$ cells/well the day prior. Infection with SARS-CoV-2 was performed using MOI of 0.1. Virus was incubated in infection media (EMEM 0% FBS) containing different concentrations of binders for 1 hr at 37°C . Culture media was removed from VeroE6 cells and 300 μL of the blocker/virus inoculum was added to cells for 1 hr at 37°C . After this step, 1 mL of EMEM with 10% FBS was added to the cells, and the cells were incubated 37°C for an additional 16 hrs before RNA harvest. Viral entry into cells and cellular transcription of viral genes was measured by qPCR using the N gene and host GUSB and host ACTB as controls. RNAeasy RNA extraction kit (Qiagen) was used for RNA extraction and Quantitect Reverse-transcriptase kit (Qiagen) was used to generate cDNA. qPCR reactions were prepared using SYBR Select Master Mix (Thermo). N gene and hGUSB gene primer concentration was 400 nM and annealing temperature was 58°C . Primer sequences (IDT) were the following – viral N gene: N_F = CACATTGGCACCCGCAATC; N_R = GAGGAACGAGAAGAGGCTTG; host gene: hGUSB_F = CTCATCTGGAATTTTGCCGATT; hGUSB_R = CCGAGTGAAGACCCCTTTT. Relative copy number (RCN) of viral transcript level compared to host transcript was determined using the ΔCT method. The half-maximal inhibitory concentration (IC_{50}) was determined using a 4-parameter nonlinear regression (GraphPad Prism).

Expression and purification of Spike ectodomain for cryo-EM

To obtain pre-fusion spike ectodomain, methods similar to the previous reports were used.^{33,50} The expression plasmid, provided by the McLellan lab, was used in a transient transfection with 100 mL, high-density Chinese Hamster Ovary (ExpiCHO, Thermo Fisher) culture following the “High Titer” protocol provided by Thermo Fisher. Six to nine days post-transfection, the supernatant was collected with centrifugation at 4,000xg at room temperature. The clarified supernatant was then incubated with Ni-Sepharose Excel resin (Cytiva Life Sciences) for ninety minutes at room temperature. After incubation, the nickel resin was washed with 20 mM Tris (pH 8), 200 mM NaCl, and 20 mM imidazole with ten column volumes. Protein was eluted from the nickel resin with 20 mM Tris (pH 8), 200 mM NaCl, and 500 mM imidazole. Eluate was then concentrated with a 50 MWCO Amicon Ultra-15 centrifugal unit by centrifugation at 2500xg, room temperature. The eluate was concentrated, filtered with a 0.2 μ m filter, and injected onto a Superose6 10/300 GL column equilibrated with 10 mM Tris (pH 8), 200 mM NaCl. The fractions corresponding to monodisperse spike were collected and the concentration was determined using a nanodrop.

Cryo-EM sample preparation, data collection and processing

2 μ M Spike ectodomain was mixed with 5-fold excess VH₃ B01 and applied (3 μ L) to holey carbon Au 200 mesh 1.2/1.3 Quantifoil grids. Grids were blotted and plunge frozen using Mark 4 Vitrobot (ThermoFisher) at 4°C and 100% humidity, utilizing blot force 0 and blot time of 4 sec. 1656 images were collected on Titan Krios (ThermoFisher) equipped with K3 direct detector operated in CDS mode (Gatan Ametek) and an energy filter (Gatan Ametek) at nominal magnification of 105000x (0.834 Å/physical pixel). Dose fractionated movies were collected with a total exposure of 6 seconds and 0.04 seconds per frame at a dose rate of 9 electrons per physical pixel per second. Movies were corrected for motion and filtered to account for electron damage utilizing MotionCor2.⁵¹ Drift corrected sums were imported into cryoSPARC2 processing package.⁵² Micrographs were manually curated, CTF was estimated utilizing patches and particles were picked with a Gaussian blob. Previous Spike ectodomain structure was imported as an initial model (low pass filtered to 30 Å) and multiple rounds of 3D and 2D classification were performed. Images were re-picked with the best looking 2D class averages low pass filtered to 30 Å, and multiple rounds of 3D classification were performed again to obtain a homogeneous stack of Spike trimer particles. Majority of the particles went into classes putatively representing excess unbound VH₃ B01 and the final Spike like particle stack only contained ~21000 particles. Non-uniform homogeneous refinement of the particle stack resulted in global resolution of 3.2 Å (masked) utilizing 0.143 FSC cut off.⁵³ PDB:6X2B was rigid body fit into the resulting reconstruction in UCSF Chimera.⁵⁴ The RBDs of two Spike trimers were moved as a rigid body to accommodate the cryo-EM density. The cryo-EM reconstruction was low pass filtered to 6 Å to better visualize the VH densities. Homology model was built based on the PDB:4G80 for the VH domains and the resulting and individual VH domains were rigid body fit into the 6 Å cryo-EM density as depicted in Fig. 5A. The resulting model was relaxed into the cryo-EM map low pass filtered to 6 Å with Rosetta FastRelax protocol. For Fig. S13 the local resolution was estimated using ResMap.⁵⁵ The final figures were prepared using ChimeraX.⁵⁶

Data availability

Cryo-EM structural data have been deposited in the Protein Data Bank and Electron Microscopy Data Bank, (PDB 7JWB and EMD-22514). The cryo-EM structure of Spike trimer from PDB:6VSB and ACE2 from PDB: 6M17 and PDB:6MOJ were used to for distance estimates. The cryo-EM structure of Spike trimer from PDB: 6X2B and crystal structure of a VH domain from PDB: 3P9W were used for cryo-EM data processing. Source data for Figures 1–4 and Extended Data Figures (2,4,5, and 7) are provided with this paper. Any additional information is available upon request.

Code availability

Code used to analyze NGS data has been deposited onto Github and is available for download at: https://github.com/crystaljie/VH_library_CDR_H3_NGS_analysis_Cole.Bracken.git.

Extended Data

CDR H1

	28	29	30	31	32	33	33a	33b	34	35	36
Template:	N	I	K	D	T	Y	-	-	I	G	W
Library:	RAD	IF	YS	YS	YSED	YSED	-	-	I	G	W
	RAD	IF	YS	YS	YS	YSED	YSED	-	I	G	W
	RAD	IF	YS	YS	YS	YSED	YSED	YSED	I	G	W

CDR H2

	49	50	51	52	52a	53	54	55	56	57	58	59
Template:	A	R	I	Y	P	T	N	G	Y	T	R	Y
Library:	A	R	I	YS	PS	YS	YS	SG	YS	T	YS	Y

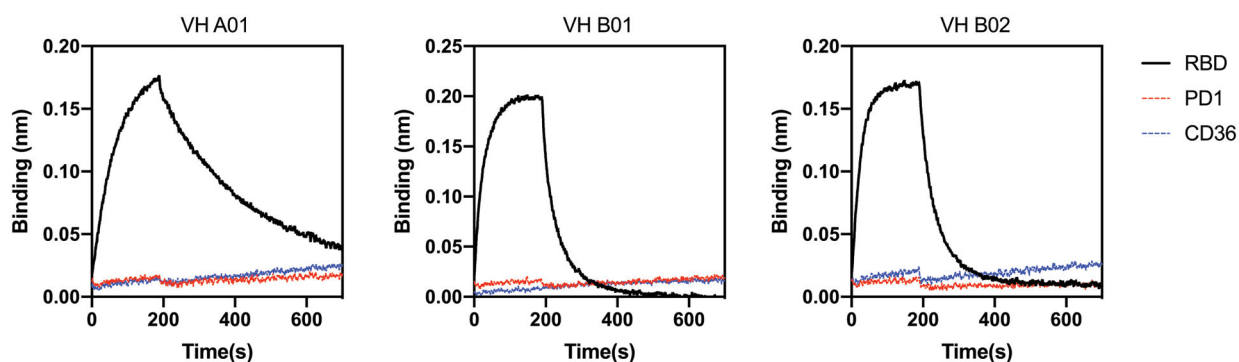
CDR H3

	94	95	96	97	98	99	100	100a	100b	100c	101	102
Template:	R	W	G	G	D	G	F	Y	A	M	D	Y
Library:	R	X ₍₂₋₁₆₎	-	-	-	-	-	-	AG	FLIM	D	Y

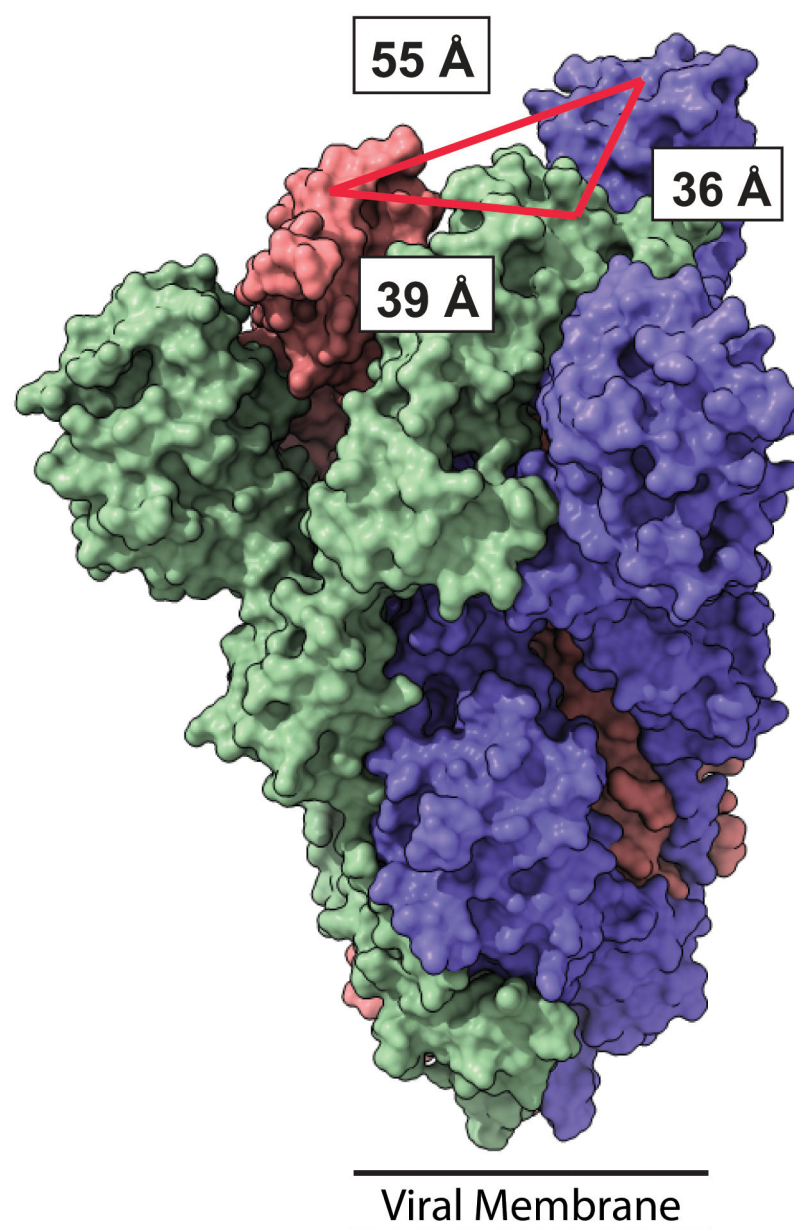
$$X = \begin{matrix} Y = 20\%, S = 17.5\%, G = 15\%, D = 10\%, A = 7.5\%, F = 7.5\%, \\ W = 7.5\%, P = 5\%, V = 5\%, H = 2.5\%, R = 2.5\% \end{matrix}$$

Extended Data Fig. 1. CDR loop design of VH-phage library

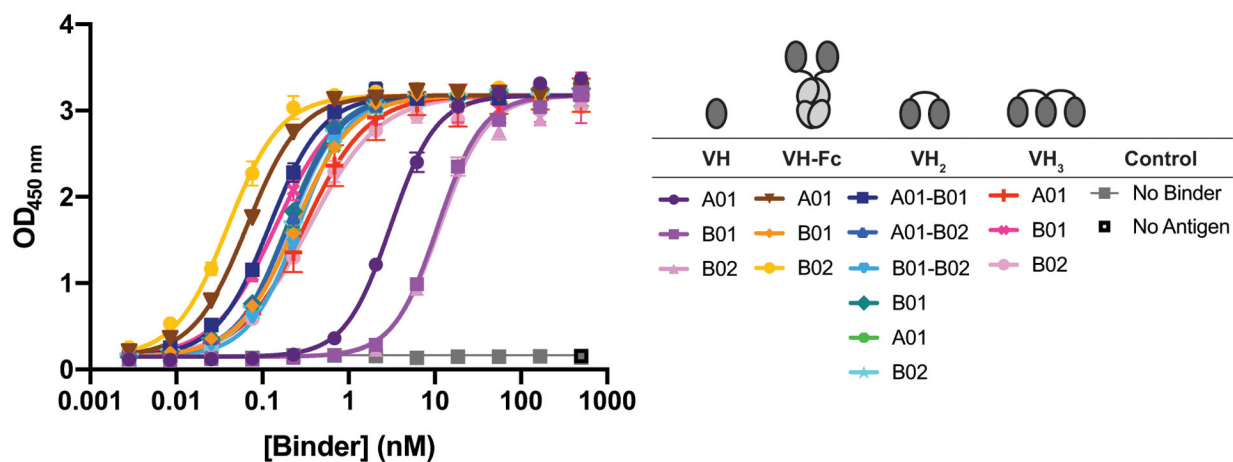
Schematic of CDR amino acid composition as compared to parental template. Positions in pink highlight CDR H1 charged amino acid insertions. Positions in blue highlight the insertion of “X” synthetic amino acid mixture. Positions in gray remain unchanged from template.

**Extended Data Fig. 2. Specificity of lead VH domain binders**

Bio-layer interferometry (BLI) binding traces of VH domains at 150nM to RBD and two decoy antigens expressed as biotinylated Fc-fusions: programmed cell death protein 1 (PD-1), and platelet glycoprotein 4 (CD36). Respective VH show successful binding to RBD, but not to either of the decoy antigens.

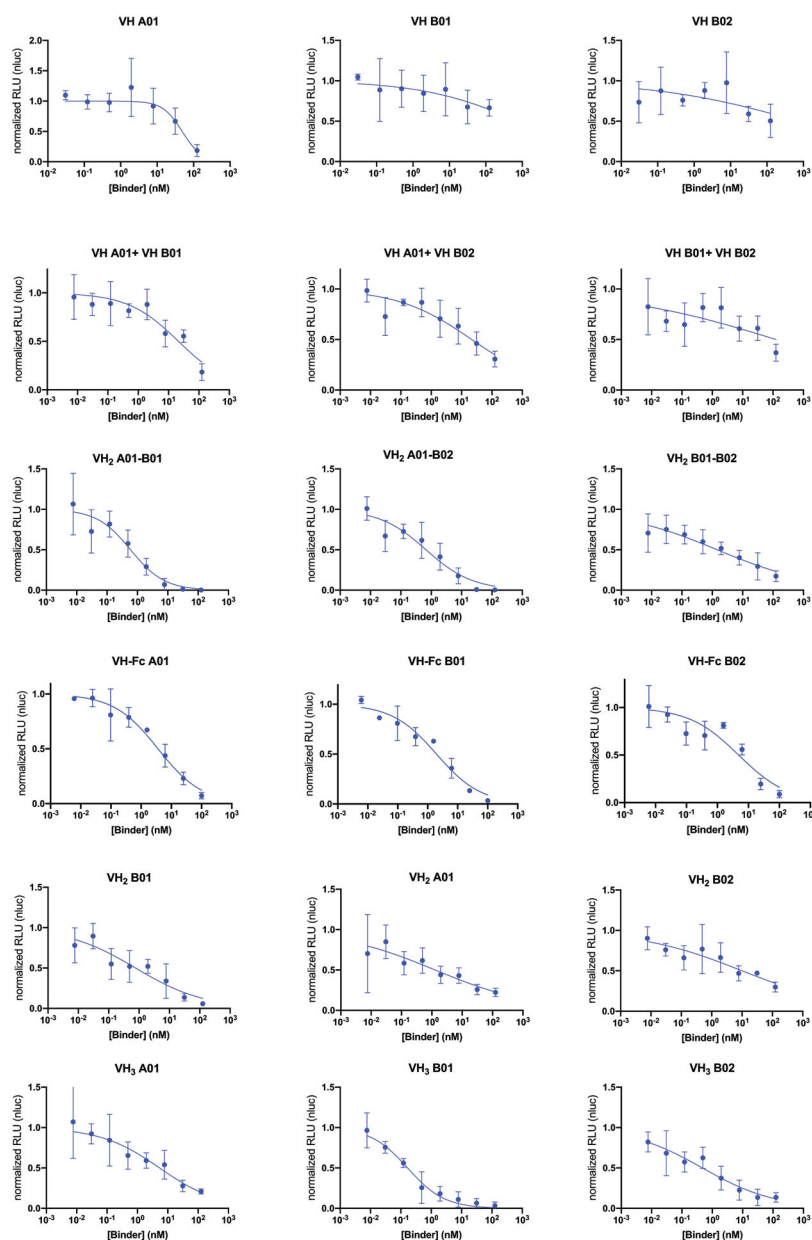


Extended Data Fig. 3. Measurements of inter-RBD distance on Spike trimer
Structure of SARS-CoV-2 Spike trimer (PDB: 6VSB)³³. RBD colored in blue is in the “up” position while RBDs colored in green and pink are in the “down” position. Distance between the mid-points of the ACE2 binding interface (PDB: 6M17)¹ on respective RBDs was measured in Pymol.



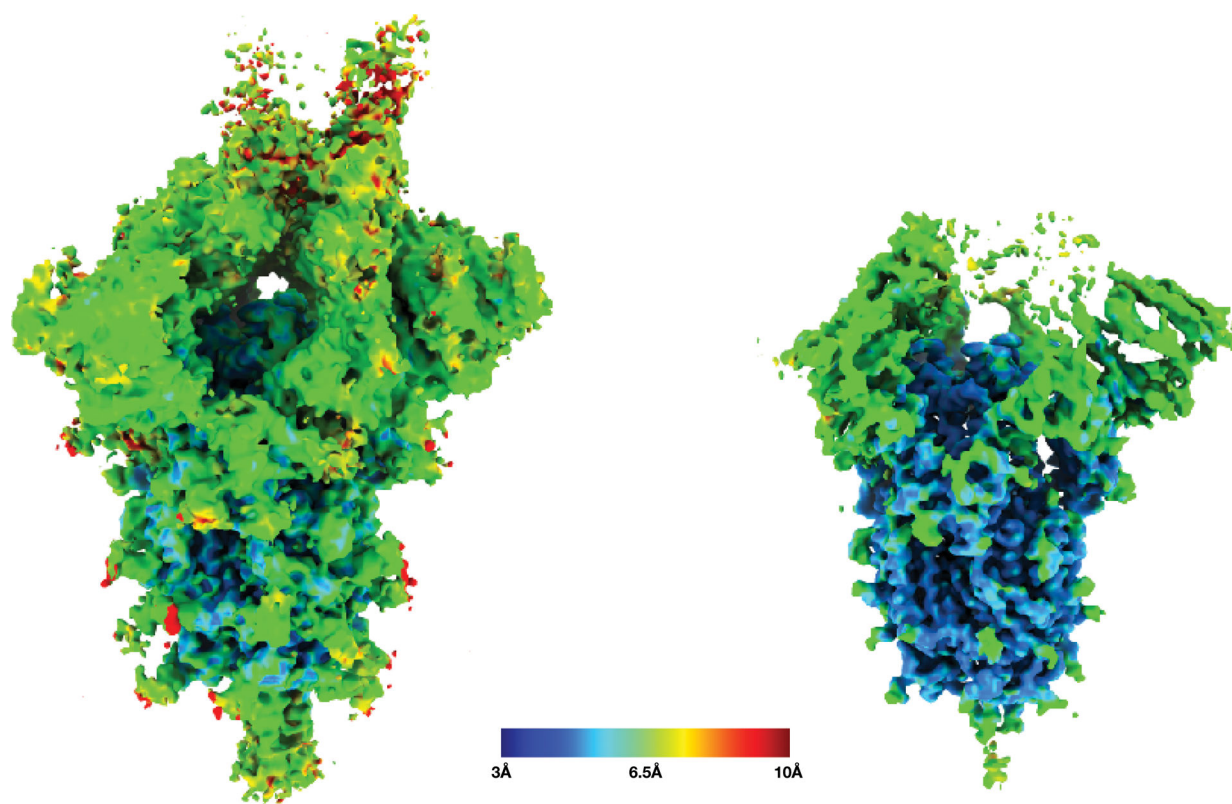
Extended Data Fig. 4. ELISA of VH binders to Spike-RBD

ELISA of VH binders against Spike-RBD. Data presented show the average and standard deviation from three independent experiments. Data were fit to a non-linear, four-parameter variable slope regression model using Prism 8 to obtain EC₅₀ values for each binder.



Extended Data Fig. 5. Pseudotyped virus neutralization by VH Binders

Pseudotyped virus neutralization assays of VH binders. Data represent average and standard deviation of two biological replicates. Data were fit to a non-linear, four-parameter variable slope regression model using Prism 8 to obtain IC_{50} values.

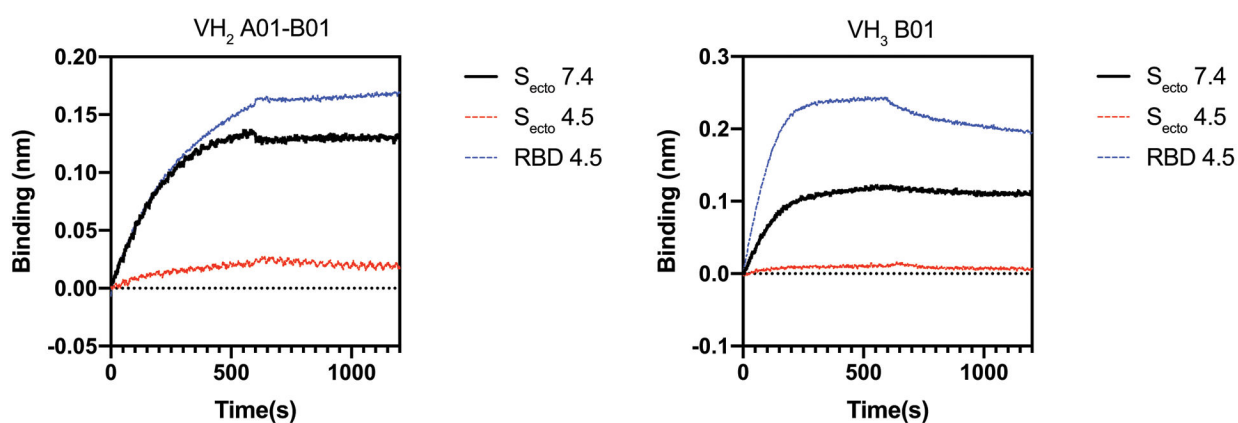


Low threshold

High threshold

Extended Data Fig. 6. Cryo-EM reconstruction of SARS-CoV-2 Spike trimer

The SARS-CoV-2 Spike trimer + VH₃ B01 cryo-EM reconstruction from non-uniform refinement in cryoSPARC at two different thresholds colored by resolution in the range from 3 Å to 10 Å. At high threshold the core S2 clearly displays high resolution features but the periphery of the molecule is closer to 6–7 Å.



Extended Data Fig. 7. pH dependent binding of lead multivalent and bi-paratopic VH

BLI assay of lead constructs at 25 nM to S_{ecto} and RBD at pH 7.4 or pH 4.5. Binding of VH leads is only observed with S_{ecto} at pH 7.4 and RBD at pH 4.5.

Supplementary Material

Refer to Web version on PubMed Central for supplementary material.

Authors

Colton J. Bracken¹, Shion A. Lim¹, Paige Solomon¹, Nicholas J. Rettko¹, Duy P. Nguyen^{1,6}, Beth Shoshana Zha², Kaitlin Schaefer¹, James R. Byrnes¹, Jie Zhou¹, Irene Lui¹, Jia Liu^{1,7}, Katarina Pance¹, QCRG Structural Biology Consortium

Caleigh M. Azumaya, Christian Billesbølle, Axel F. Brilot, Melody G. Campbell, Amy Diallo, Miles Sasha Dickinson, Devan Diwanji, Meghna Gupta, Nadia Herrera, Nick Hoppe, Huong T. Kratochvil, Yanxin Liu, Gregory E. Merz, Henry C. Nguyen, Carlos Nowotny, Michelle Moritz, Tristan W. Owens, Sergei Pourmal, Cristina Puchades, Alexandria N. Rizo, Ursula Schulze-Gahmen, Amber M. Smith, Ming Sun, Erron W. Titus, Iris D. Young, Jianhua Zhao, Daniel Asarnow, Justin Biel, Alisa Bowen, Julian R. Braxton, David Bulkley, Jen Chen, Cynthia M. Chio, Un Seng Chio, Ishan Deshpande, Loan Doan, Bryan Faust, Sebastian Flores, Mingliang Jin, Kate Kim, Victor L. Lam, Fei Li, Junrui Li, Yen-Li Li, Yang Li, Xi Liu, Megan Lo, Kyle E. Lopez, Liam McKay, Arthur A. Melo, Frank R. Moss III, Phuong Nguyen, Joana Paulino, Komal Ishwar Pawar, Jessica K. Peters, Thomas H. Pospiech Jr., Maliheh Safari, Smriti Sangwan, Kaitlin Schaefer, Mariano Tabios, Paul V. Thomas, Aye C. Thwin, Raphael Trenker, Donovan Trinidad, Eric Tse, Tsz Kin Martin Tsui, Feng Wang, Natalie Whitis, Zanlin Yu, Kaihua Zhang, Yang Zhang, Fengbo Zhou, Oren S Rosenberg, Kliment A Verba, David A Agard, Yifan Cheng, James S Fraser, Adam Frost, Natalia Jura, Tanja Kortemme, Nevan J Krogan, Aashish Manglik, Daniel R. Southworth, Robert M Stroud

³, Xin X. Zhou¹, Kevin K. Leung¹, James A. Wells^{1,4,5,*}

Caleigh M. Azumaya, Christian Billesbølle, Axel F. Brilot, Melody G. Campbell, Amy Diallo, Miles Sasha Dickinson, Devan Diwanji, Meghna Gupta, Nadia Herrera, Nick Hoppe, Huong T. Kratochvil, Yanxin Liu, Gregory E. Merz, Henry C. Nguyen, Carlos Nowotny, Michelle Moritz, Tristan W. Owens, Sergei Pourmal, Cristina Puchades, Alexandria N. Rizo, Ursula Schulze-Gahmen, Amber M. Smith, Ming Sun, Erron W. Titus, Iris D. Young, Jianhua Zhao, Daniel Asarnow, Justin Biel, Alisa Bowen, Julian R. Braxton, David Bulkley, Jen Chen, Cynthia M. Chio, Un Seng Chio, Ishan Deshpande, Loan Doan, Bryan Faust, Sebastian Flores, Mingliang Jin, Kate Kim, Victor L. Lam, Fei Li, Junrui Li, Yen-Li Li, Yang Li, Xi Liu, Megan Lo, Kyle E. Lopez, Liam McKay, Arthur A. Melo, Frank R. Moss III, Phuong Nguyen, Joana Paulino, Komal Ishwar Pawar, Jessica K. Peters, Thomas H. Pospiech Jr., Maliheh Safari, Smriti Sangwan, Kaitlin Schaefer, Mariano Tabios, Paul V. Thomas, Aye C. Thwin, Raphael Trenker, Donovan Trinidad, Eric Tse, Tsz Kin Martin Tsui, Feng Wang, Natalie Whitis, Zanlin Yu, Kaihua Zhang, Yang Zhang, Fengbo Zhou, Oren S Rosenberg, Kliment A Verba, David A Agard, Yifan Cheng, James S Fraser, Adam

Frost, Natalia Jura, Tanja Kortemme, Nevan J Krogan, Aashish Manglik, Daniel R. Southworth, Robert M Stroud

Affiliations

¹Department of Pharmaceutical Chemistry, University of California San Francisco, San Francisco, California, 94158, USA.

²Department of Pulmonary, Critical Care, Allergy and Sleep Medicine, University of California San Francisco, San Francisco, CA 94158, USA.

³Quantitative Biosciences Institute (QBI) Coronavirus Research Group Structural Biology Consortium, University of California San Francisco, San Francisco, CA 94158, USA.

⁴Department of Cellular & Molecular Pharmacology, University of California San Francisco, San Francisco, California, 94158, USA.

⁵Chan Zuckerberg Biohub, San Francisco, CA 94158, USA

⁶Present address: Lyell Immunopharma Inc., Seattle, WA 98109, USA

⁷Present address: Merck & Co., South San Francisco, CA 94080, USA

Acknowledgements:

We thank members of the Wells Lab, particularly those working on COVID-19 projects for their efforts and contributions. Specifically, we would like to thank J. Grimespacher for purifying binders and M. Nix (UCSF) for guidance on pseudotyped virus neutralization assays. Additionally, we thank the entire QCRG for its rapid large-scale collaborative effort. Specifically, we thank C. Puchades and C. Azumaya for their efforts in the optimization of cryo-EM grid freezing and data collection; T. Owens for assistance in protein purification; D. Diwanji for expression of Secto; and A. Manglik (UCSF) for advice on cryo-EM experiments and protein purification. We also thank the laboratory of P. Kim (Stanford University) for providing plasmids for pseudotyped virus production. Lastly, we thank M. Wilson, C. Chiu, and R. Loudermilk (UCSF) as well as the patients, for providing convalescent sera.

J.A.W. is supported by generous grants from NCI (R35 GM122451-01); Chan-Zuckerberg Biohub, UCSF Program for Breakthrough Biomedical Research (PBBR); Fast Grants from Emergent Ventures at the Mercatus Center, George Mason University (#2154); and funding from The Harrington Discovery Institute (GA33116). S.A.L. is a Merck Fellow of the Helen Hay Whitney Foundation. K.S. is a Fellow of the Helen Hay Whitney Foundation. X.X.Z. is a Merck Fellow of the Damon Runyon Cancer Research Foundation, DRG-2297-17. J.R.B. and J.Z. are supported by a National Institutes of Health National Cancer Institute F32 5F32CA239417 (to J.R.B.) and 5F32CA236151-02 (to J.Z.). B.S.Z. is supported by a National Institutes of Health National Cancer Institute T32 (HL007185). N.J.R. and I.L. are supported by the National Science Foundation (GRFP). D.P.N. was the Connie and Bob Lurie Fellow of the Damon Runyon Cancer Research Foundation (DRG-2204-14) and supported by a UCSF-PBBR Postdoctoral Independent Research Award, which is partially funded by the Sandler Foundation.

Main Text References

1. Yan Ret al. Structural basis for the recognition of SARS-CoV-2 by full-length human ACE2. *Science* 367, 1444–1448 (2020). [PubMed: 32132184]
2. Abraham J Passive antibody therapy in COVID-19. *Nat. Rev. Immunol* 20, 401–403 (2020). [PubMed: 32533109]
3. Robbiani D Fet al. Convergent antibody responses to SARS-CoV-2 in convalescent individuals. *Nature* 584, 437–442 (2020). [PubMed: 32555388]
4. Pinto Det al. Cross-neutralization of SARS-CoV-2 by a human monoclonal SARS-CoV antibody. *Nature* 583, 290–295 (2020). [PubMed: 32422645]

5. Rogers TF et al. Isolation of potent SARS-CoV-2 neutralizing antibodies and protection from disease in a small animal model. *Science* 7520, eabc7520 (2020).
6. Cao Yet al. Potent neutralizing antibodies against SARS-CoV-2 identified by high-throughput single-cell sequencing of convalescent patients' B cells. *Cell* 182, 73–84 (2020). [PubMed: 32425270]
7. Shi Ret al. A human neutralizing antibody targets the receptor binding site of SARS-CoV-2. *Nature* 584, 120–124 (2020). [PubMed: 32454512]
8. Miersch Set al. Scalable high throughput selection from phage-displayed synthetic antibody libraries. *J. Vis. Exp* 1–15 (2015). doi:10.3791/51492
9. Nguyen VK, Hamers R, Wyns L & Muyldermans S Camel heavy-chain antibodies: Diverse germline V(H)H and specific mechanisms enlarge the antigen-binding repertoire. *EMBO J.* 19, 921–930 (2000). [PubMed: 10698934]
10. Holt LJ, Herring C, Jespers LS, Woolven BP & Tomlinson IM Domain antibodies: Proteins for therapy. *Trends Biotechnol.* 21, 484–490 (2003). [PubMed: 14573361]
11. Ingram JR, Schmidt FI & Ploegh HL Exploiting Nanobodies' Singular Traits. *Annu. Rev. Immunol* 36, (2018).
12. Hamer-Casterman Atarchouch TC, et al. Naturally occurring antibodies devoid of light chains. *Nature* 363, 446–448 (1998).
13. De Genst E et al. Molecular basis for the preferential cleft recognition by dromedary heavy-chain antibodies. *Proc. Natl. Acad. Sci. U. S. A* 103, 4586–4591 (2006). [PubMed: 16537393]
14. Arbabi-Ghahroudi M, Tanha J & MacKenzie R Prokaryotic expression of antibodies. *Cancer Metastasis Rev.* 24, 501–519 (2005). [PubMed: 16408159]
15. Zimmermann I et al. Synthetic single domain antibodies for the conformational trapping of membrane proteins. *Elife* 7, 1–32 (2018).
16. McMahon C et al. Yeast surface display platform for rapid discovery of conformationally selective nanobodies. *Nat. Struct. Mol. Biol* 25, 289–296 (2018). [PubMed: 29434346]
17. Saerens D, Ghassabeh GH & Muyldermans S Single-domain antibodies as building blocks for novel therapeutics. *Curr. Opin. Pharmacol* 8, 600–608 (2008). [PubMed: 18691671]
18. Nilvebrant J, Tessier P & Sidhu S Engineered Autonomous Human Variable Domains. *Curr. Pharm. Des* 22, 6527–6537 (2016). [PubMed: 27655414]
19. Rouet R, Dudgeon K, Christie M, Langley D & Christ D Fully human VH single domains that rival the stability and cleft recognition of camelid antibodies. *J. Biol. Chem* 290, 11905–11917 (2015). [PubMed: 25737448]
20. Sun Z et al. Potent neutralization of SARS-CoV-2 by human antibody heavy-chain variable domains isolated from a large library with a new stable scaffold. *MAbs* 12, 1778435 (2020). [PubMed: 32544372]
21. Cao Yet al. Potent Neutralizing Antibodies against SARS-CoV-2 Identified by High-Throughput Single-Cell Sequencing of Convalescent Patients' B Cells. *Cell* 182, 73–84 (2020). [PubMed: 32425270]
22. Huo J et al. Neutralizing nanobodies bind SARS-CoV-2 spike RBD and block interaction with ACE2. *Nat. Struct. Mol. Biol* 27, 846–854 (2020). [PubMed: 32661423]
23. Walter J D et al. Sybodies targeting the SARS-CoV-2 receptor-binding domain. *BioRxiv* (2020). doi:10.1101/2020.04.16.045419
24. Palomo C et al. Trivalency of a nanobody specific for the human respiratory syncytial virus fusion glycoprotein drastically enhances virus neutralization and impacts escape mutant selection. *Antimicrob. Agents Chemother* 60, 6498–6509 (2016). [PubMed: 27550346]
25. Carter P et al. Humanization of an anti-p185HER2 antibody for human cancer therapy. *Proc. Natl. Acad. Sci. U. S. A* 89, 4285–4289 (1992). [PubMed: 1350088]
26. Harmsen M M et al. Llama heavy-chain V regions consist of at least four distinct subfamilies revealing novel sequence features. *Mol. Immunol* 37, 579–590 (2000). [PubMed: 11163394]
27. Ma X, Barthelemy PA, Rouge L, Wiesmann C & Sidhu S S Design of synthetic autonomous VH domain libraries and structural analysis of a VH domain bound to vascular endothelial growth factor. *J. Mol. Biol* 425, 2247–2259 (2013). [PubMed: 23507309]

28. Dudgeon Ket al. General strategy for the generation of human antibody variable domains with increased aggregation resistance. *Proc. Natl. Acad. Sci. U. S. A* 109, 10879–10884 (2012). [PubMed: 22745168]
29. Birtalan Set al. The Intrinsic Contributions of Tyrosine, Serine, Glycine and Arginine to the Affinity and Specificity of Antibodies. *J. Mol. Biol* 377, 1518–1528 (2008). [PubMed: 18336836]
30. Hornsby Met al. A High Through-put Platform for Recombinant Antibodies to Folded Proteins. *Mol. Cell. Proteomics* 14, 2833–2847 (2015). [PubMed: 26290498]
31. Martinko A Jet al. Targeting RAS-driven human cancer cells with antibodies to upregulated and essential cell-surface proteins. *Elife* 7, e31098 (2018). [PubMed: 29359686]
32. Kabat EA, Wu TT, Reid-Miller M, Perry H, Gottesman K Sequences of proteins of immunological interest. National Institutes of Health, Bethesda, MD, U.S.A. (1987). doi:10.1016/0003-2697(84)90805-4
33. Wrapp Det al. Cryo-EM structure of the 2019-nCoV spike in the prefusion conformation. *Science* 367, 1260–1263 (2020). [PubMed: 32075877]
34. Lui I et al. Trimeric SARS-CoV-2 Spike interacts with dimeric ACE2 with limited intra-Spike avidity. *BioRxiv* (2020). doi:10.1101/2020.05.21.109157
35. Neuman BW et al. Supramolecular Architecture of Severe Acute Respiratory Syndrome Coronavirus Revealed by Electron Cryomicroscopy. *J. Virol* 80, 7918–7928 (2006). [PubMed: 16873249]
36. Byrnes J Ret al. Competitive SARS-CoV-2 Serology Reveals Most Antibodies Targeting the Spike Receptor-Binding Domain Compete for ACE2 Binding. *mSphere* 5, e00802–20 (2020).
37. Crawford KH Det al. Protocol and reagents for pseudotyping lentiviral particles with SARS-CoV-2 spike protein for neutralization assays. *Viruses* 12, 513 (2020).
38. Walls AC et al. Structure, Function, and Antigenicity of the SARS-CoV-2 Spike Glycoprotein. *Cell* 180, 281–292 (2020).
39. Zhou Tet al. A pH-dependent switch mediates conformational masking of SARS-CoV-2 spike. *BioRxiv* (2020). doi:10.1101/2020.07.04.187989
40. Lan Jet al. Structure of the SARS-CoV-2 spike receptor-binding domain bound to the ACE2 receptor. *Nature* 581, 215–220 (2020). [PubMed: 32225176]
41. Dong Jet al. Development of multi-specific humanized llama antibodies blocking SARS-CoV-2/ACE2 interaction with high affinity and avidity. *Emerg. Microbes Infect* 9, 1034–1036 (2020). [PubMed: 32403995]
42. Binz HK, Amstutz P & Plückthun A Engineering novel binding proteins from nonimmunoglobulin domains. *Nat. Biotechnol* 23, 1257–1268 (2005). [PubMed: 16211069]
43. Binz HK, Stumpp MT, Forrer P, Amstutz P & Plückthun A Designing repeat proteins: Well-expressed, soluble and stable proteins from combinatorial libraries of consensus ankyrin repeat proteins. *J. Mol. Biol* 332, 489–503 (2003). [PubMed: 12948497]
44. Binz HK et al. Design and characterization of MP0250, a tri-specific anti-HGF/anti-VEGF DARPin® drug candidate. *MAbs* 9, 1262–1269 (2017). [PubMed: 29035637]
45. Conrath KE, Lauwereys M, Wyns L & Muyldermans S Camel Single-domain Antibodies as Modular Building Units in Bispecific and Bivalent Antibody Constructs. *J. Biol. Chem* 276, 7346–7350 (2001). [PubMed: 11053416]
46. Strauch E Met al. Computational design of trimeric influenza-neutralizing proteins targeting the hemagglutinin receptor binding site. *Nat. Biotechnol* 35, 667–671 (2017). [PubMed: 28604661]
47. Galimidi RP et al. Intra-spike crosslinking overcomes antibody evasion by HIV-1. *Cell* 160, 433–446 (2015). [PubMed: 25635457]
48. Lee CV et al. High-affinity human antibodies from phage-displayed synthetic Fab libraries with a single framework scaffold. *J. Mol. Biol* 340, 1073–1093 (2004). [PubMed: 15236968]
49. Chen G & Sidhu SS Design and generation of synthetic antibody libraries for phage display. *Methods Mol. Biol* 1131, 113–131 (2014). [PubMed: 24515463]
50. Wang B et al. Bivalent binding of a fully human IgG to the SARS-CoV-2 spike proteins reveals mechanisms of potent neutralization. *BioRxiv* (2020). doi:10.1101/2020.07.14.203414
51. Zheng S Q et al. MotionCor2: Anisotropic correction of beam-induced motion for improved cryo-electron microscopy. *Nat. Methods* 14, 331–332 (2017). [PubMed: 28250466]

52. Punjani A, Rubinstein JL, Fleet DJ & Brubaker MA CryoSPARC: Algorithms for rapid unsupervised cryo-EM structure determination. *Nat. Methods* 14, 290–296 (2017). [PubMed: 28165473]
53. Punjani A, Zhang H & Fleet DJ Non-uniform refinement: Adaptive regularization improves single particle cryo-EM reconstruction. *BioRxiv* (2019). doi:10.1101/2019.12.15.877092
54. Pettersen EF et al. UCSF Chimera - A visualization system for exploratory research and analysis. *J. Comput. Chem* 25, 1605–1612 (2004). [PubMed: 15264254]
55. Kucukelbir A, Sigworth FJ & Tagare HD Quantifying the local resolution of cryo-EM density maps. *Nat. Methods* 11, 63–65 (2014). [PubMed: 24213166]
56. Goddard TD et al. UCSF ChimeraX: Meeting modern challenges in visualization and analysis. *Protein Sci.* 27, 14–25 (2018). [PubMed: 28710774]

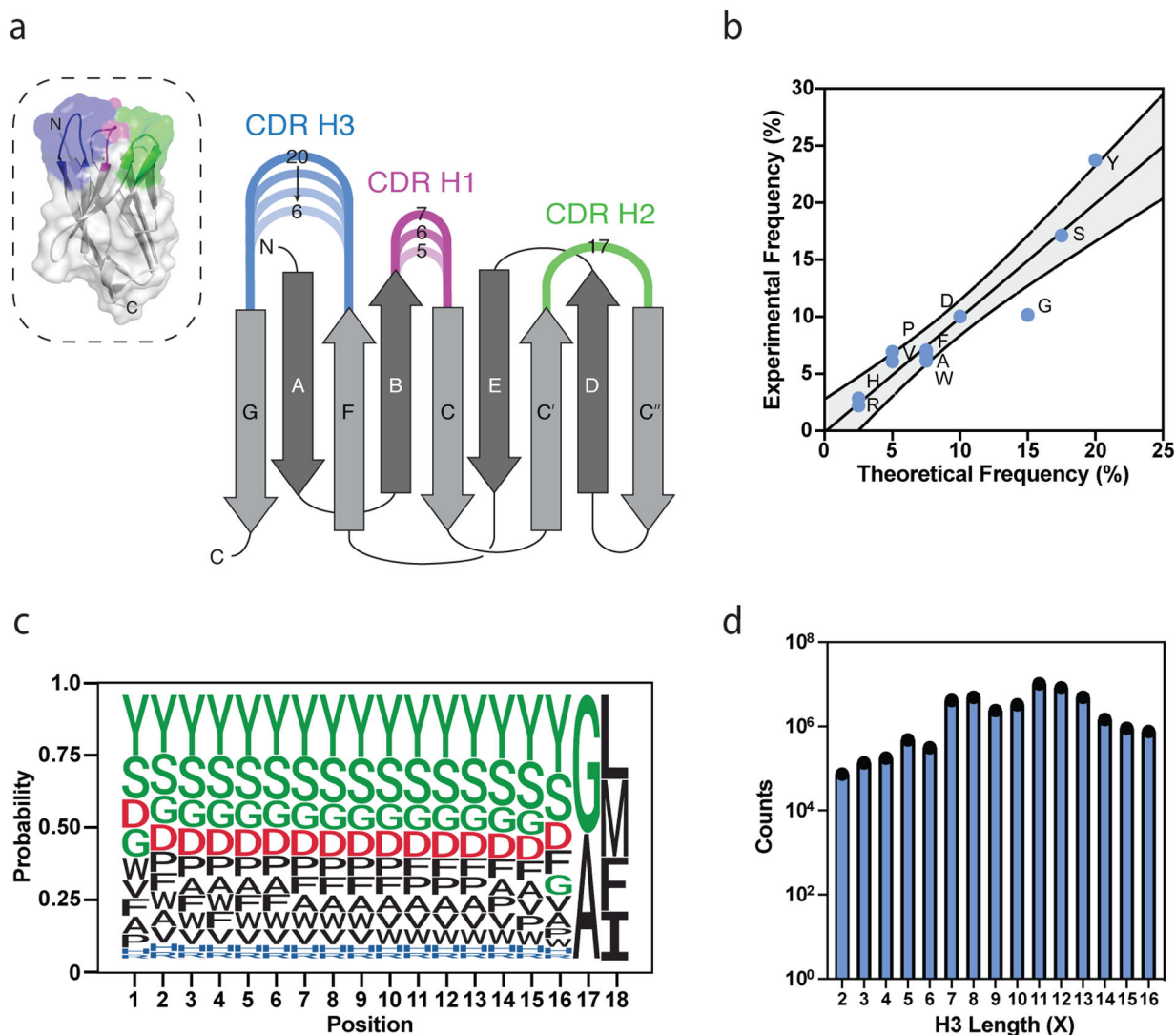


Figure 1: Design and validation of VH-phage library

(A) 3D surface representation (left) of the VH-4D5 parental scaffold (PDB:1FVC) and a cartoon diagram (right) where individual CDRs are annotated in color with the designed loop length variations according to Kabat nomenclature.³² (B) NGS analysis of the longest H3 loop (X=16) shows that expected global amino acid frequencies are comparable to designed frequencies. Gray region denotes the 95% confidence interval. (C) Representative NGS analysis of the longest H3 loop (X=16) shows positional frequency distribution matches designed frequencies. Position 1 refers to residue 95 (Kabat definition). Data for the other CDR H3 lengths are reported in Fig. S2. (D) NGS analysis of unique clones shows that all H3 lengths are represented in the pooled VH-phage library.

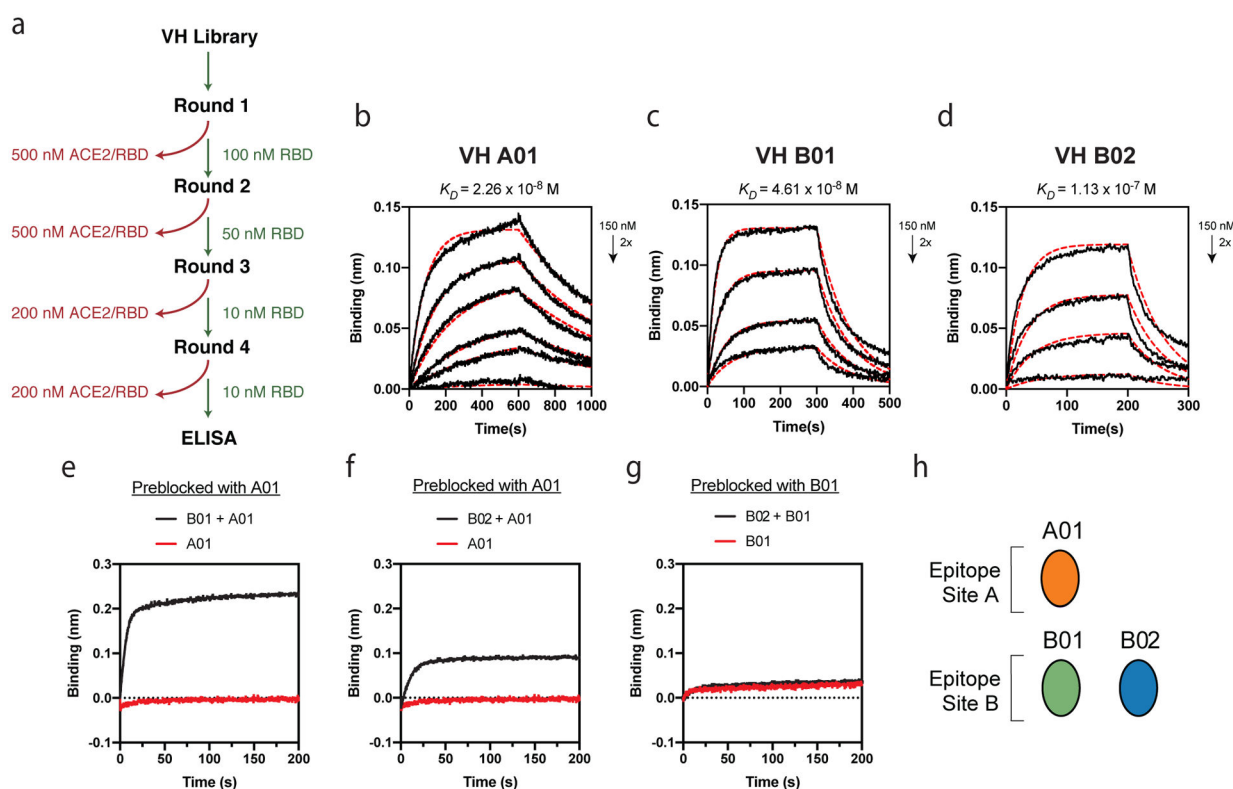


Figure 2: Identification of VH domains that bind Spike-RBD at two unique epitopes by phage display

(A) Diagram illustrating phage selection strategy to isolate VH-phage that bind at the ACE2 binding interface. Red indicates clearance of the phage pool by Spike-RBD-Fc/ACE2-Fc complex, green indicates positive selection against Spike-RBD-Fc alone. To increase stringency, successively lower concentrations of Spike-RBD-Fc were used, and after 4 rounds of selection, individual phage clones were analyzed by phage ELISA. BLI of (B) VH A01 (C) VH B01 and (D) VH B02 against Spike-RBD. (E) BLI-based epitope binning of VH A01 and VH B01, (F) VH A01 and VH B02, (G) VH B01 and VH B02. The antigen loaded onto the sensor tip was Spike-RBD. (H) Diagram of the two different epitope bins targeted by VH domains.

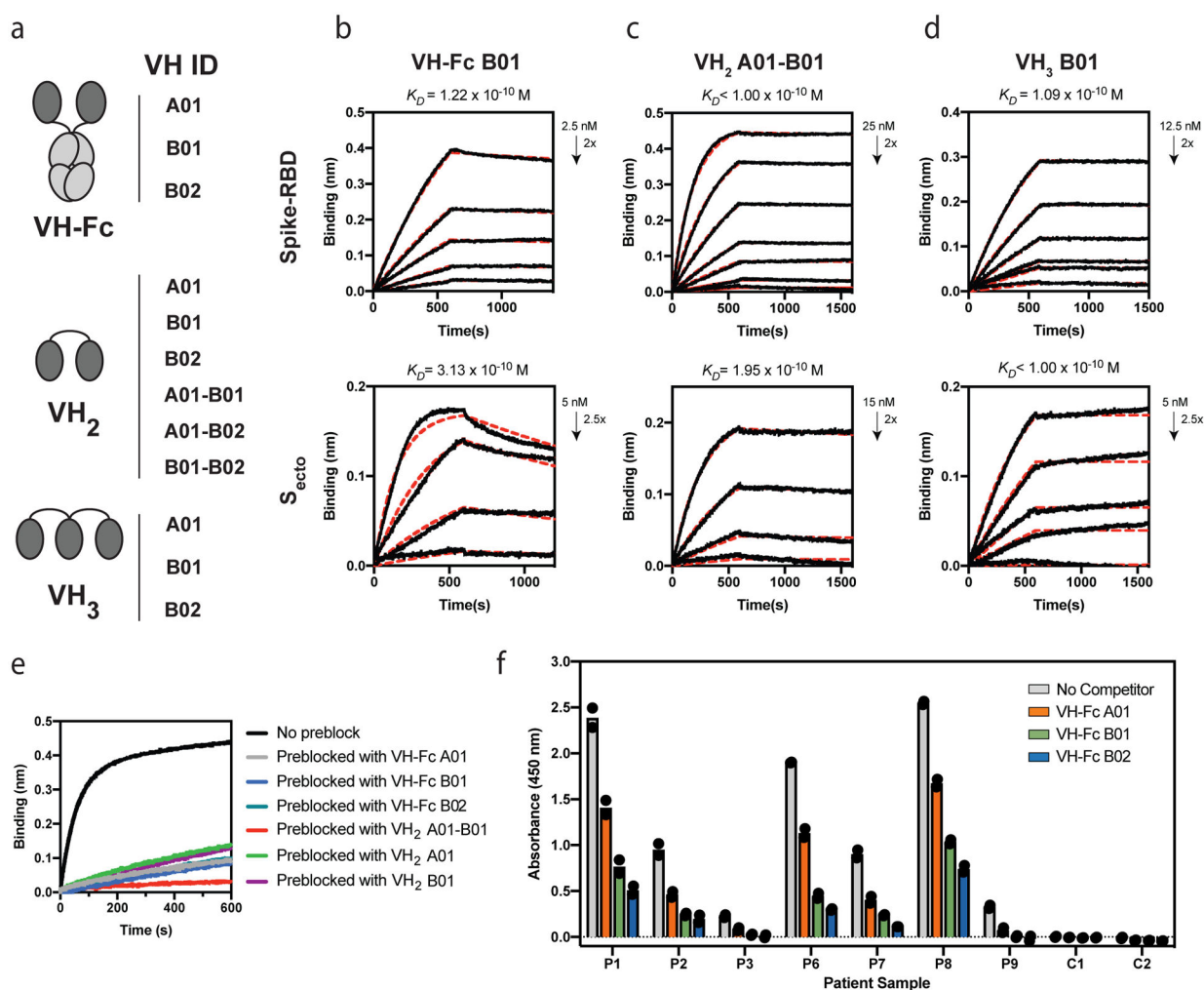


Figure 3: In vitro characterization of multivalent and bi-paratopic VH binders

(A) Cartoon depiction of engineered VH binders generated by linking VH domains via Fc-fusion or a 20-aa Gly-Ser linker. BLI traces of lead VH binders, (B) VH-Fc B01, (C) VH₂ A01-B01, (D) VH₃ B01 against RBD (upper panel) or S_{ecto} (lower panel). (E) Sequential BLI binding experiments that measured binding of ACE2-Fc to S_{ecto} pre-blocked with our VH binders show that multivalent VH binders can block ACE2-Fc binding to S_{ecto}. (F) Competition serology ELISA with convalescent patient sera indicates that VH-Fc binders can compete with patient antibodies. P1-P9 are sera from patients with a history of prior SARS-CoV-2 infection. C1-C2 are two donor sera collected before the SARS-CoV-2 outbreak. Individual data points represent technical replicates (n=2) from the serum of the same patient and are shown as black circles.

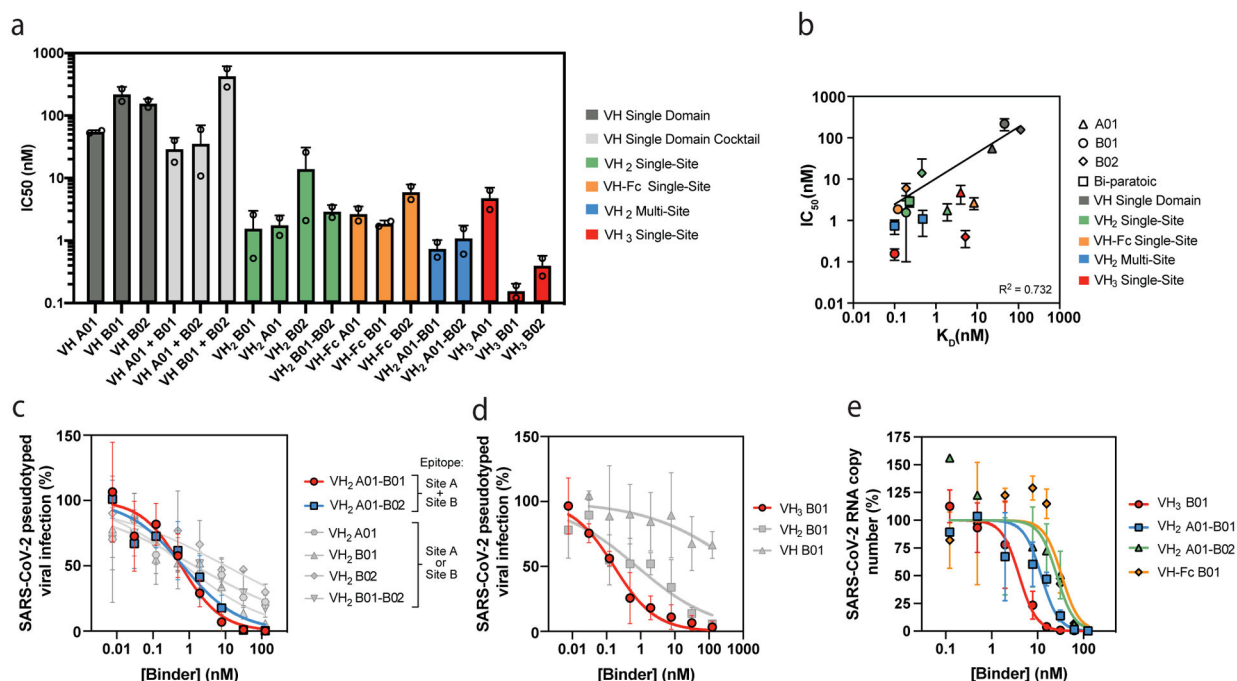


Figure 4: Multivalent and bi-paratopic VH binders neutralize pseudotyped and authentic SARS-CoV-2

(A) Pseudotyped virus IC₅₀ of VH binders. Neutralization potency improves when VH domains are engineered into multivalent and bi-paratopic constructs. (B) Correlation of in vitro binding affinity (K_D) and pseudotyped virus neutralization (IC₅₀) of VH binders. Data were fit to a log-log linear extrapolation. (C) Pseudotyped virus neutralization curves of multi-site VH₂ in comparison to single-site VH₂ demonstrate that the multi-site VH₂ have a more cooperative neutralization curve. (D) Pseudotyped virus neutralization curves of mono-, bi-, and tri-valent formats of VH B01 demonstrate potency gains driven by valency. (E) Authentic SARS-CoV-2 neutralization curves for the most potent VH formats were determined via qPCR of viral genome in cellular RNA. All pseudoviral neutralization data were repeated as n=2 independent replicates. Authentic virus neutralization data were repeated as n=2 independent replicates. Data represent the average and standard deviation of replicates.

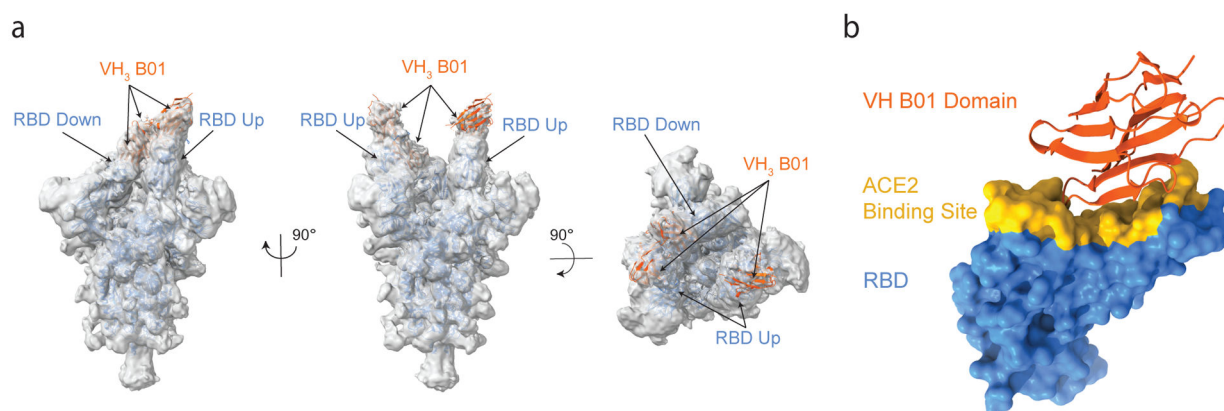


Figure 5: Cryo-EM reveals trivalent VH binding at the ACE2 binding interface of RBD
(A) Side and top views of cryo-EM 3D reconstructions of VH₃ B01 + S_{ecto} (PDB: 7JWB) are shown with individual VH domain densities of VH₃ B01 fit with PDB: 3P9W (VH scaffold; orange cartoon). A total of three VH domains, each bound to an RBD of the Spike trimer, are resolved. 3D model of S_{ecto} was fit with reference structure (PDB:6X2B with additional rigid body fit of the individual RBDs; blue cartoon) and shows RBDs in a distinct two “up”, one “down” conformation. Cryo-EM map was low-pass filtered to 6 Å. **(B)** View of the epitope (Site B) of one VH domain from VH₃ B01. Site B overlays directly with the ACE2 binding site (yellow surface; contacts defined as RBD residues within 8 Å of an ACE2 residue from PDB:6M0J).